A Proposal to Build a MiniBooNE Near Detector:BooNE

3 November, 2011

R. Dharmapalan, S. Habib, & I. Stancu
University of Alabama, Tuscaloosa, AL 35487

Z. Djurcic
Argonne National Laboratory, Argonne, IL 60439

D. Smith
Embry-Riddle Aeronautical University, Prescott, AZ 86301

L. Bartoszek, F. G. Garcia, T. Kobilarcik, W. Marsh, C. D. Moore
D. Perevalov, D. Schmitz, & G. P. Zeller
Fermi National Accelerator Laboratory, Batavia, IL 60510

J. Grange, J. Mousseau, B. Osmanov, & H. Ray
University of Florida, Gainesville, FL 32611

R. Tayloe
Indiana University, Bloomington, IN 47405

G. T. Garvey, W. Huelsnitz, W. C. Louis, G. B. Mills, Z. Pavlovic
R. Van de Water, & D. H. White
Los Alamos National Laboratory, Los Alamos, NM 87545

B. P. Roe
University of Michigan, Ann Arbor, MI 48109

A. A. Aguilar-Arevalo
Instituto de Ciencias Nucleares, Universidad Nacional Autnoma de México, México D.F. México

E. Church
Yale University, New Haven, CT 06520

1. Executive Summary

There is accumulating evidence for antineutrino oscillations at the $\Delta m^2 \sim 1$ eV^2 mass scale. In addition to an unexplained low-energy excess [1)], the MiniBooNE experiment observes an excess of electron-like events in antineutrino mode [2)] that is consistent with $\bar{\nu}_\mu \rightarrow \bar{\nu}_e$ oscillations at ~ 1 eV^2 and consistent with the evidence for oscillations from LSND [3)]. Furthermore, an improved determination of the reactor neutrino event rate is now $\sim 6\%$ higher than the world short-baseline reactor data [4)] and consistent with $\bar{\nu}_e$ disappearance at ~ 1 eV^2. These data together with the rest

of the world antineutrino data can be explained very well by a 3+1 sterile neutrino model [5]. Furthermore, the world neutrino plus antineutrino data can be explained fairly well by a 3+2 sterile neutrino model with CP violation [6,7].

In order to prove whether these event excesses are due to neutrino oscillations and whether there is CP violation in the lepton sector at short baseline, we propose building a second MiniBooNE detector at a distance of $\sim$ 200 m from the Booster Neutrino Beam (BNB) production target. With identical detectors at different distances, most of the systematic errors will cancel when taking a ratio of events in the two detectors, as the neutrino flux varies as $1/r^2$ to a calculable approximation. This will allow sensitive tests of oscillations for both ν_e and $\bar{\nu}_e$ appearance and ν_μ and $\bar{\nu}_\mu$ disappearance. Furthermore, a comparison between oscillations in neutrino mode and antineutrino mode will allow a sensitive search for CP violation in the lepton sector at short baseline ($\Delta m^2 > 0.1$ eV^2). Finally, by comparing the rates for a neutral current (NC) reaction, either NC π^0 scattering or NC elastic scattering, a direct search for sterile neutrinos will be made. The initial amount of running time requested for the near detector will be a total of $\sim$ 2E20 POT divided between neutrino mode and antineutrino mode, which will provide statistics comparable to what has already been collected in the far detector. A thorough understanding of this short-baseline physics will be of great importance to future long-baseline oscillation experiments.

The data of BooNE and MicroBooNE will address nearly all aspects of the present MiniBooNE event excess anomalies in the context of complex sterile-neutrino oscillation models or photon-like processes.

2. Introduction

Evidence for neutrino oscillations comes from solar-neutrino [8,9,10,11,12] and reactor-antineutrino experiments [13], which have observed ν_e disappearance at $\Delta m^2 \sim 7 \times 10^{-5}$ eV^2, and atmospheric-neutrino [14,15,16,17] and long-baseline accelerator-neutrino experiments [18,19], which have observed ν_μ disappearance at $\Delta m^2 \sim 2 \times 10^{-3}$ eV^2. In addition, the LSND experiment [3] has presented evidence for $\bar{\nu}_\mu \rightarrow \bar{\nu}_e$ oscillations at the $\Delta m^2 \sim 1$ eV^2 scale, as shown in Fig. 1. If all three phenomena are caused by neutrino oscillations, then these three Δm^2 scales cannot be accommodated within an extension of the Standard Model with only three neutrino mass eigenstates. An explanation of all three mass scales with neutrino oscillations requires the addition of one or more sterile neutrinos [5,6,7] or further extensions of the Standard Model [20,21].

The MiniBooNE experiment was designed to test the neutrino oscillation interpretation of the LSND signal in both neutrino and antineutrino modes. MiniBooNE has approximately the same L/E_ν as LSND but with an order of magnitude higher baseline and energy. Due to the higher energy and dissimilar event signature, MiniBooNE systematic errors are completely different from LSND errors. MiniBooNE's oscillation results in neutrino mode [22] show no significant excess of events at higher energies; however, a sizeable excess of events is observed at lower energies, as shown in Fig. 2. Although the excess energy shape does not fit well to simple two-neutrino oscilla-

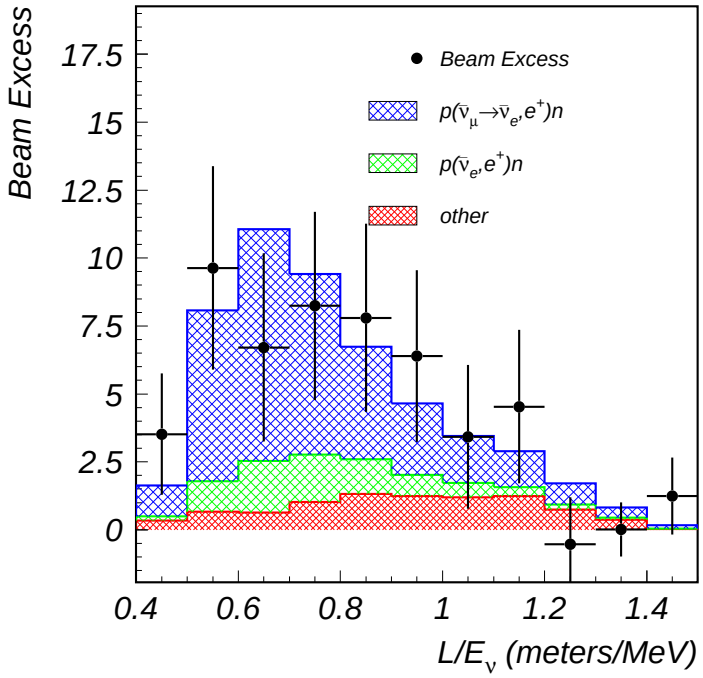

Figure 1: *The excess of $\bar{\nu}_e$ candidate events observed by the LSND experiment as a function of L/E.*

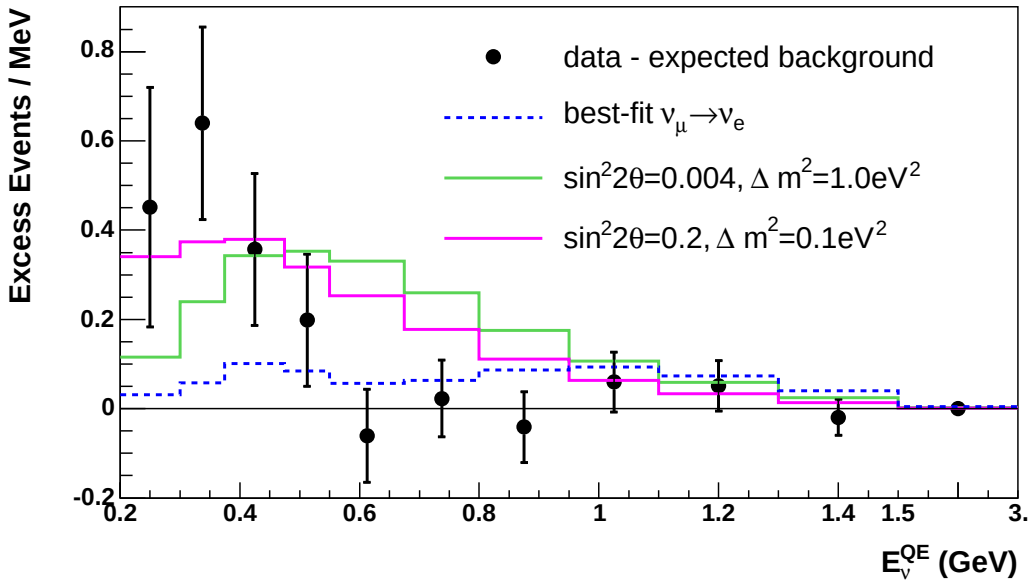

Figure 2: *The excess of ν_e candidate events observed by MiniBooNE in neutrio mode.*

tions, the number of excess events, $151.0 \pm 28.3 \pm 50.7$ events in the $200 < E_\nu < 1250$ MeV energy range, agrees approximately with the LSND expectation. At present, with 8.58E20 POT in antineutrino mode, MiniBooNE observes an event excess, $54.9 \pm 17.4 \pm 16.3$ events in the $200 < E_\nu < 1250$ MeV energy range, that is consistent with the antineutrino oscillations suggested by the LSND data [3]. Fig. 3 shows the excess of $\bar{\nu}_e$ candidate events in antineutrino mode, while Figs. 4 and 5 show that the MiniBooNE oscillation allowed region and L/E distribution agree well with LSND.

Additional evidence for short-baseline neutrino oscillations comes from the "reactor neutrino anomaly". As shown in Fig. 6, an improved determination of the reactor neutrino event rate is now $\sim 6\%$ higher than the world short-baseline reactor data [4]. This suppression is consistent with $\bar{\nu}_e$ oscillations into sterile neutrinos at a $\Delta m^2 \sim 1$ eV^2.

Global fits to the world neutrino oscillation data have been performed in terms of 3+1 and 3+2 sterile neutrino models [5,6,7]. As shown in Fig. 7, the world antineutrino data fit well [5] to a 3+1 sterile neutrino model. The best antineutrino fit occurs at $\Delta m^2_{41} = 0.92$ eV^2 with $\sin^2 2\theta_{\mu e} = 0.0045$, $\sin^2 2\theta_{\mu\mu} = 0.24$, $\sin^2 2\theta_{ee} = 0.067$, and a χ^2 probability = 92%. Global 3+N fits to the world neutrino and antineutrino data show tension between the two sets of data; however, this tension is greatly reduced when CP violation is allowed with $N > 1$. Fig. 8 shows the allowed regions for ν_e and $\bar{\nu}_e$ appearance from a global fit to the world neutrino and antineutrino data [6], assuming a 3+2 sterile neutrino model with a CP violation parameter, δ. The best fit occurs at $\Delta m^2_{41} = 0.47$ eV^2, $\Delta m^2_{51} = 0.87$ eV^2, and $\delta = 1.64\pi$ with a χ^2 probability = 90%.

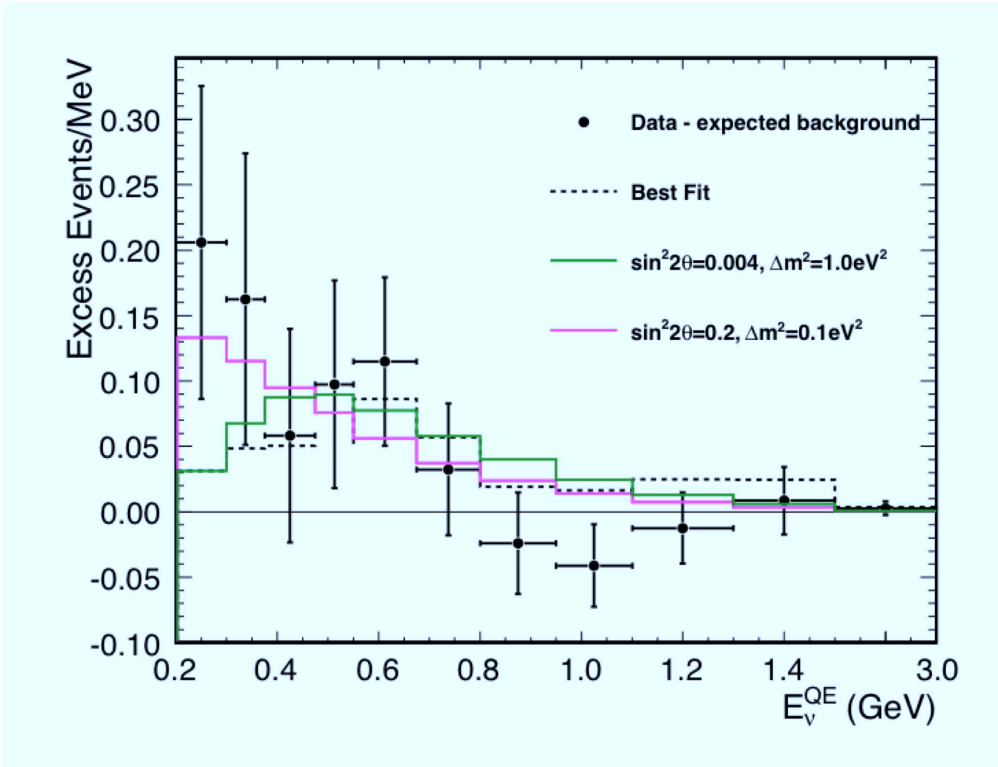

Figure 3: *The excess of $\bar{\nu}_e$ candidate events observed by MiniBooNE in antineutrino mode. The data is compared to the predictions of naive two-neutrino models*

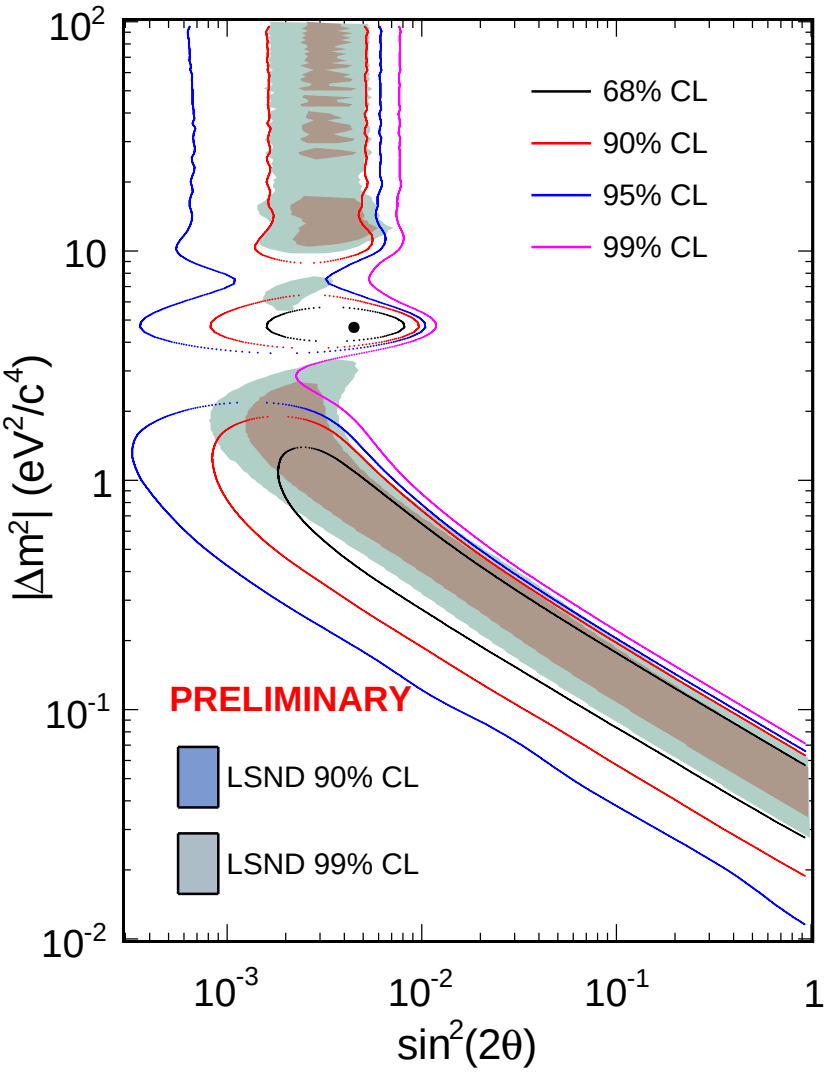

Figure 4: *The MiniBooNE oscillation allowed region in antineutrino mode agrees well with LSND in a naive two-neutrino model.*

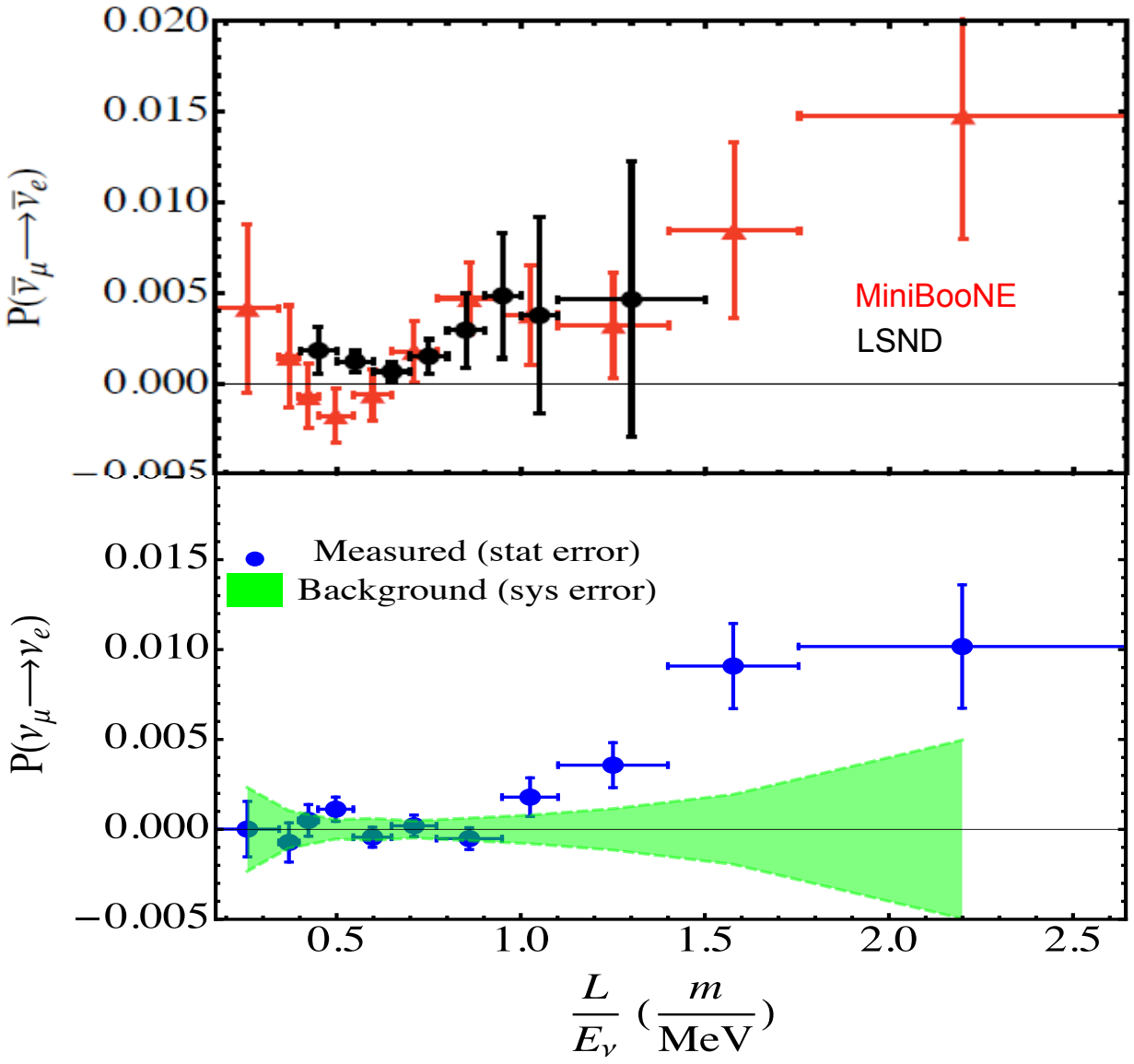

Figure 5: *In the top frame, the inferred ocillation probability is plotted versus L/E for MiniBooNE antineutrino mode data (red data points), which agrees well with LSND antineutrino data (black data points). The bottom frame shows the same distribution for neutrino mode (blue data points) with statistcal errors only. The green band indicates the size of the systematic error on the background in neutrino mode.*

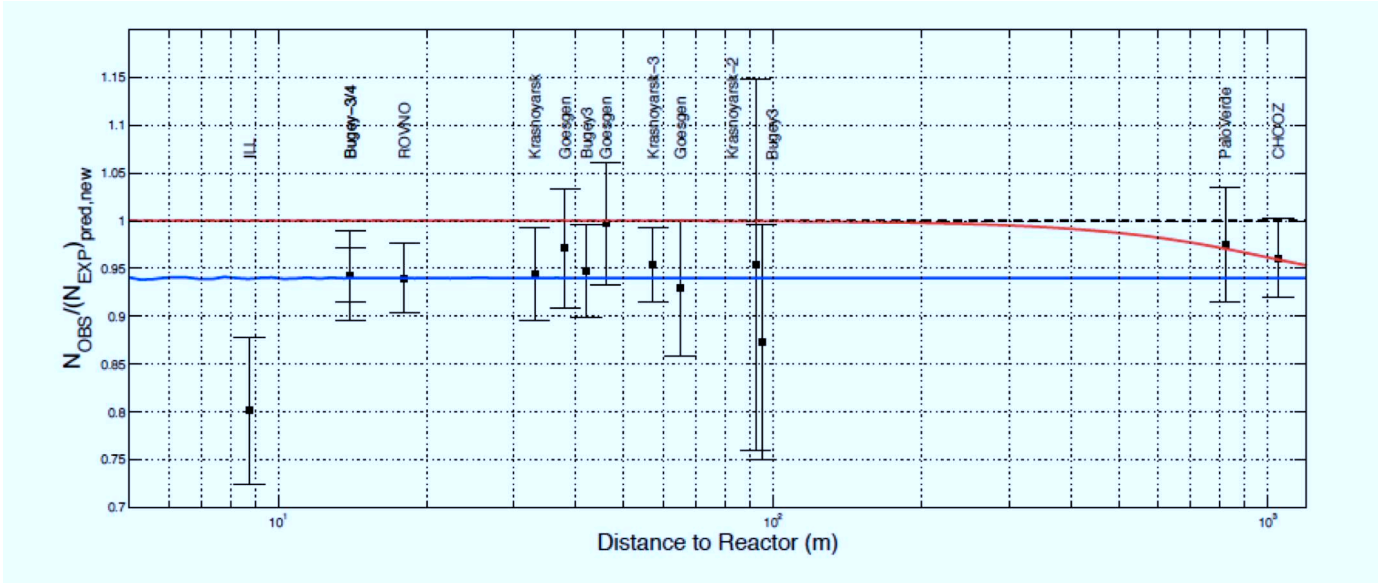

1

Figure 6: *The ratio of observed reactor neutrino event rates compared to the expectation from an improved determination of the rate. The world short-baseline reactor data are about 6% lower than the estimate (blue curve). The red curve is the expected event rate with a non-zero value of* θ_{13}.

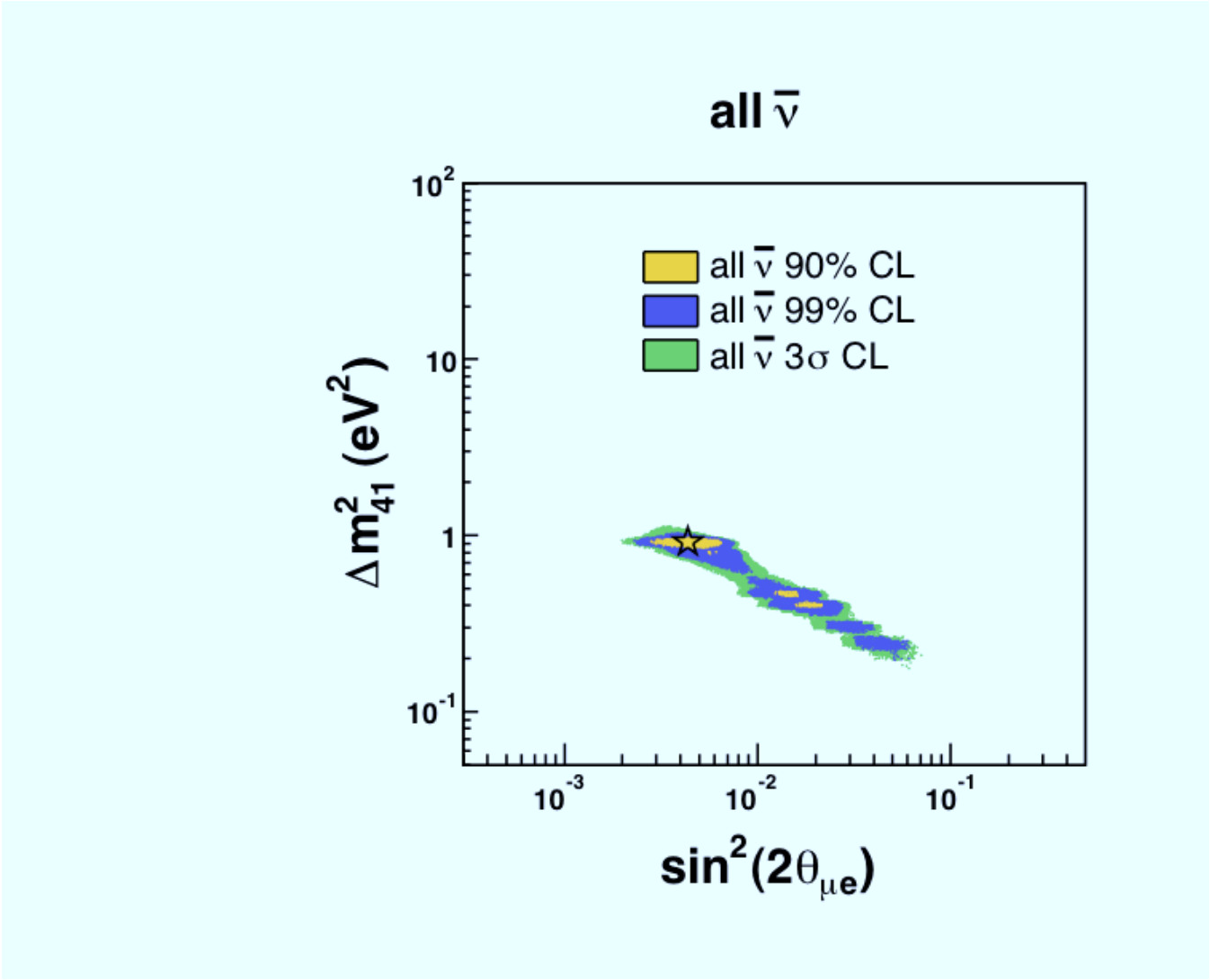

Figure 7: *The allowed region for $\bar{\nu}_e$ appearance from a global fit to the world antineutrino data by Karagiorgi et al., assuming a 3+1 sterile antineutrino model. The star indicates the best-fit point at $\Delta m^2_{41} = 0.92\ eV^2$ and $\sin^2 2\theta_{\mu e} = 0.0045$.*

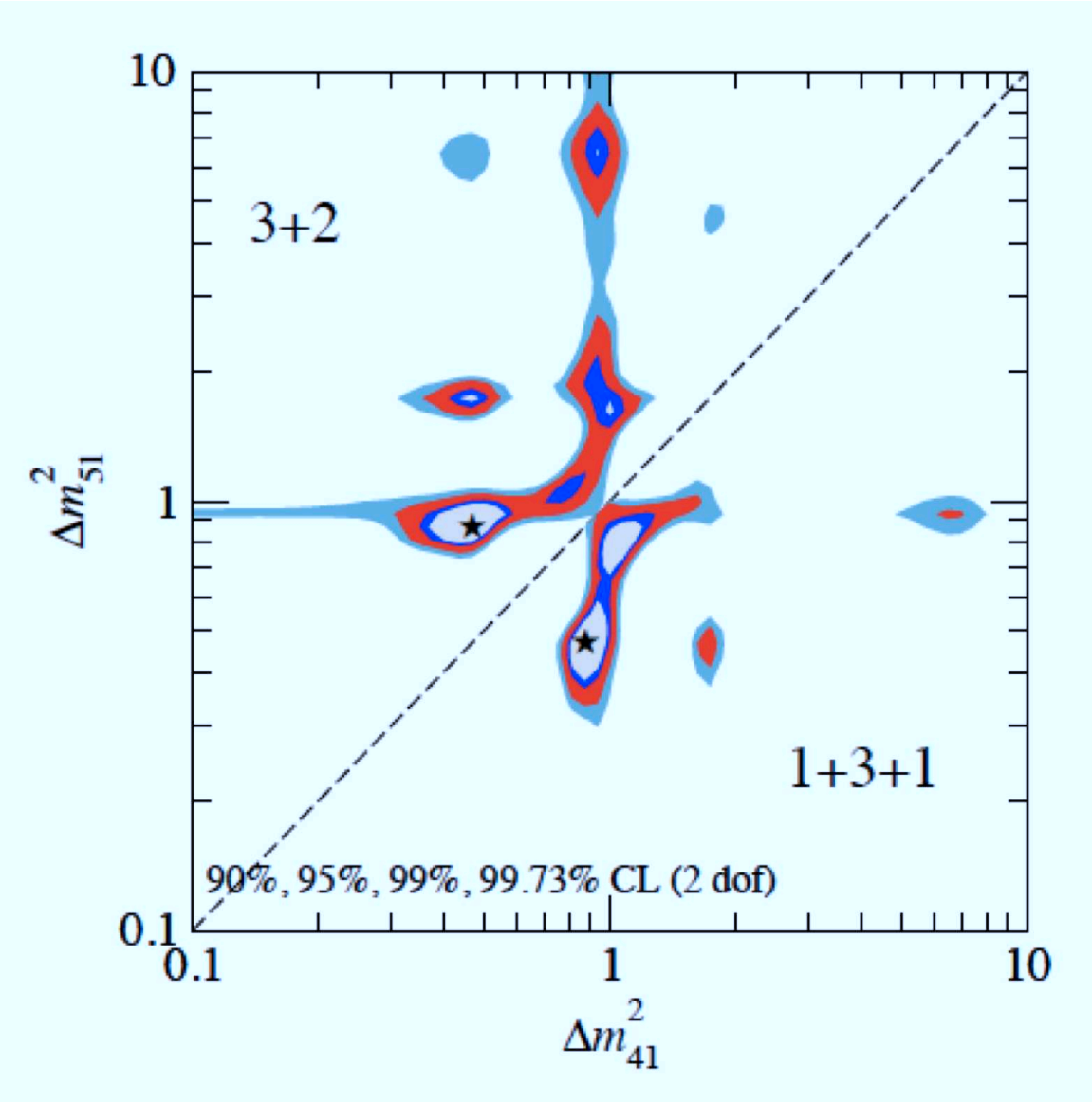

Figure 8: *The allowed region for ν_e and $\bar{\nu}_e$ appearance from a global fit to the world neutrino and antineutrino data by Kopp, Maltoni, and Schwetz, assuming a 3+2 sterile neutrino model with CP violation. The star indicates the best-fit point at $\Delta m^2_{41} = 0.47\ eV^2$ and $\Delta m^2_{51} = 0.87\ eV^2$. For the 1+3+1 model, the lightest and heaviest neutrinos are mostly sterile. For the 3+2 model, the two heaviest neutrinos are mostly sterile.*

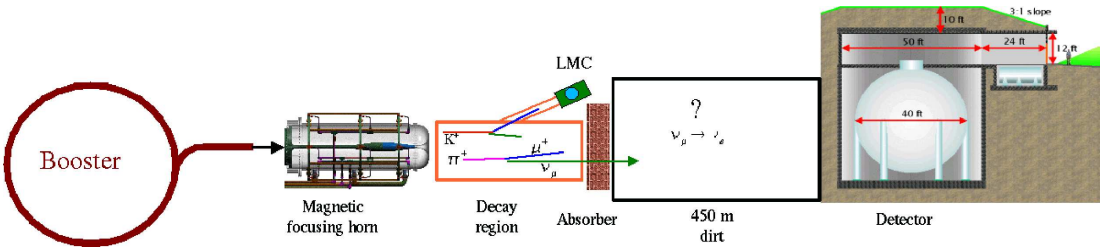

Figure 9: *A schematic drawing of the MiniBooNE experiment.*

3. MiniBooNE

3.1. Description of the Experiment

A schematic drawing of the MiniBooNE experiment at FNAL is shown in Fig. 9. The experiment is fed by 8-GeV kinetic energy protons from the Booster that interact in a 71-cm long Be target located at the upstream end of a magnetic focusing horn. The horn pulses with a current of 174 kA and, depending on the polarity, either focuses π^+ and K^+ and defocuses π^- and K^- to form a pure neutrino beam or focuses π^- and K^- and defocuses π^+ and K^+ to form a somewhat pure antineutrino beam. The produced pions and kaons decay in a 50-m long pipe, and a fraction of the neutrinos and antineutrinos [23] interact in the MiniBooNE detector, which is located 541 m downstream of the Be target. For the MiniBooNE results presented here, a total of 6.5×10^{20} POT were collected in neutrino mode and 8.58×10^{20} POT have been collected so far in antineutrino mode.

The MiniBooNE detector [24] consists of a 12.2-m diameter spherical tank filled with approximately 800 tons of mineral oil (CH_2). A schematic drawing of the MiniBooNE detector is shown in Fig. 10. There are a total of 1280 8-inch detector phototubes (covering 10% of the surface area) and 240 veto phototubes. The fiducial volume has a 5-m radius and corresponds to approximately 450 tons. Only $\sim 2\%$ of the phototube channels failed so far over the course of the run. Fig. 11 shows that the MiniBooNE event rate per POT has been very stable over the life of the experiment.

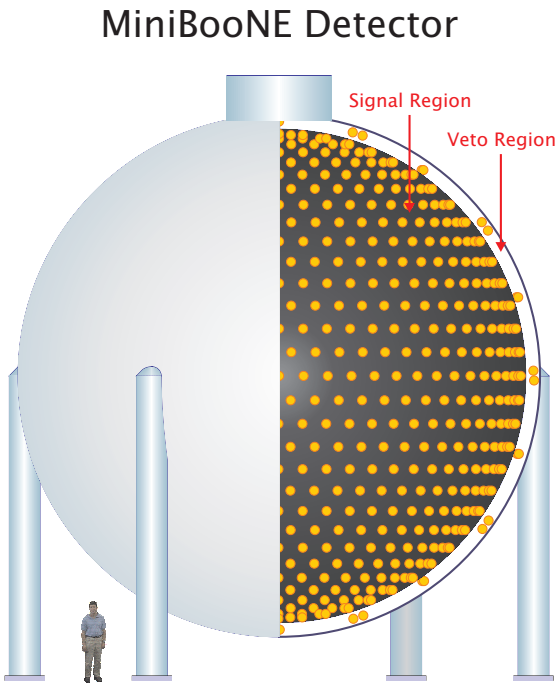

Figure 10: *A schematic drawing of the MiniBooNE detector.*

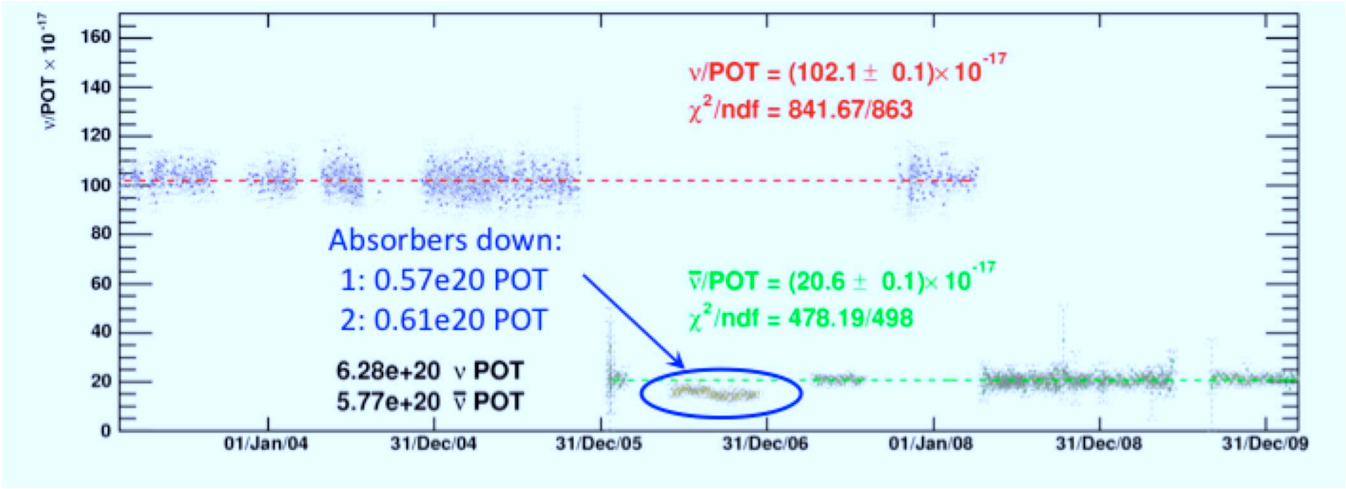

Figure 11: *The MiniBooNE event rate per POT has been very stable over the life of the experiment.*

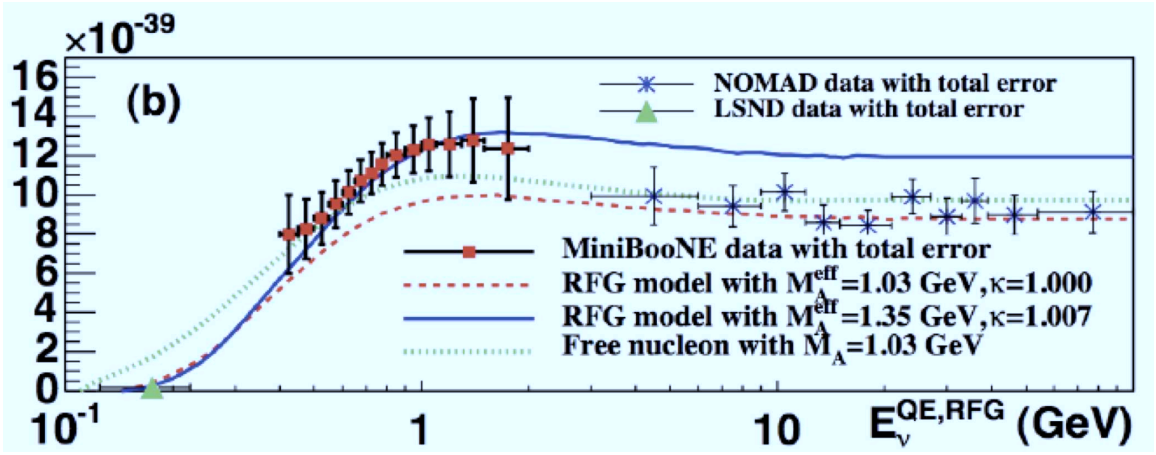

Figure 12: *The MiniBooNE ν_μ CCQE cross section measurement as a function of neutrino energy.*

3.2. MiniBooNE Cross Section Results

MiniBooNE has published many cross section results, including the first double-differential measurement of ν_μ charged-current quasi-elastic (CCQE) scattering [25]. As shown in Fig. 12, the MiniBooNE ν_μ CCQE cross section on carbon is not only higher than the expectation from the relativistic Fermi Gas model but also higher than the cross section off six free neutrons, which is a very surprising result! How can this be? How can the cross section off bound neutrons be higher than the cross section off free neutrons? A possible explanation involves short-range correlations and pion-exchange currents, which have been observed in electron scattering [26] and proposed as an explanation for the enhanced MiniBooNE cross section [27,28]. From these MiniBooNE cross section measurements, it is now clear that the Fermi Gas Model is inadequate for neutrino-nucleus inclusive scattering and that realistic models are required that have to include initial and final state correlations and two-body currents. Those nuclear correlations play an important role in the reconstruction of neutrino energies in present and future neutrino oscillation experiments. For example, neutrino energies that are derived incorrectly from measured muon energies and directions could significantly bias fitted oscillation parameters.

MiniBooNE has also collected the world's largest event samples of neutral-current elastic scattering [29], charged-current π^+ production [30], charged-current π^0 production [31] production, and neutral-current π^0 production [32]. Fig. 13 summarizes the MiniBooNE single pion cross section measurements. Also, by fitting the $\gamma\gamma$ mass and $E_\pi(1-\cos\theta_\pi)$ distributions, the fraction of π^0 produced coherently is determined to be $19.5 \pm 1.1 \pm 2.5\%$, as shown in Fig. 14.

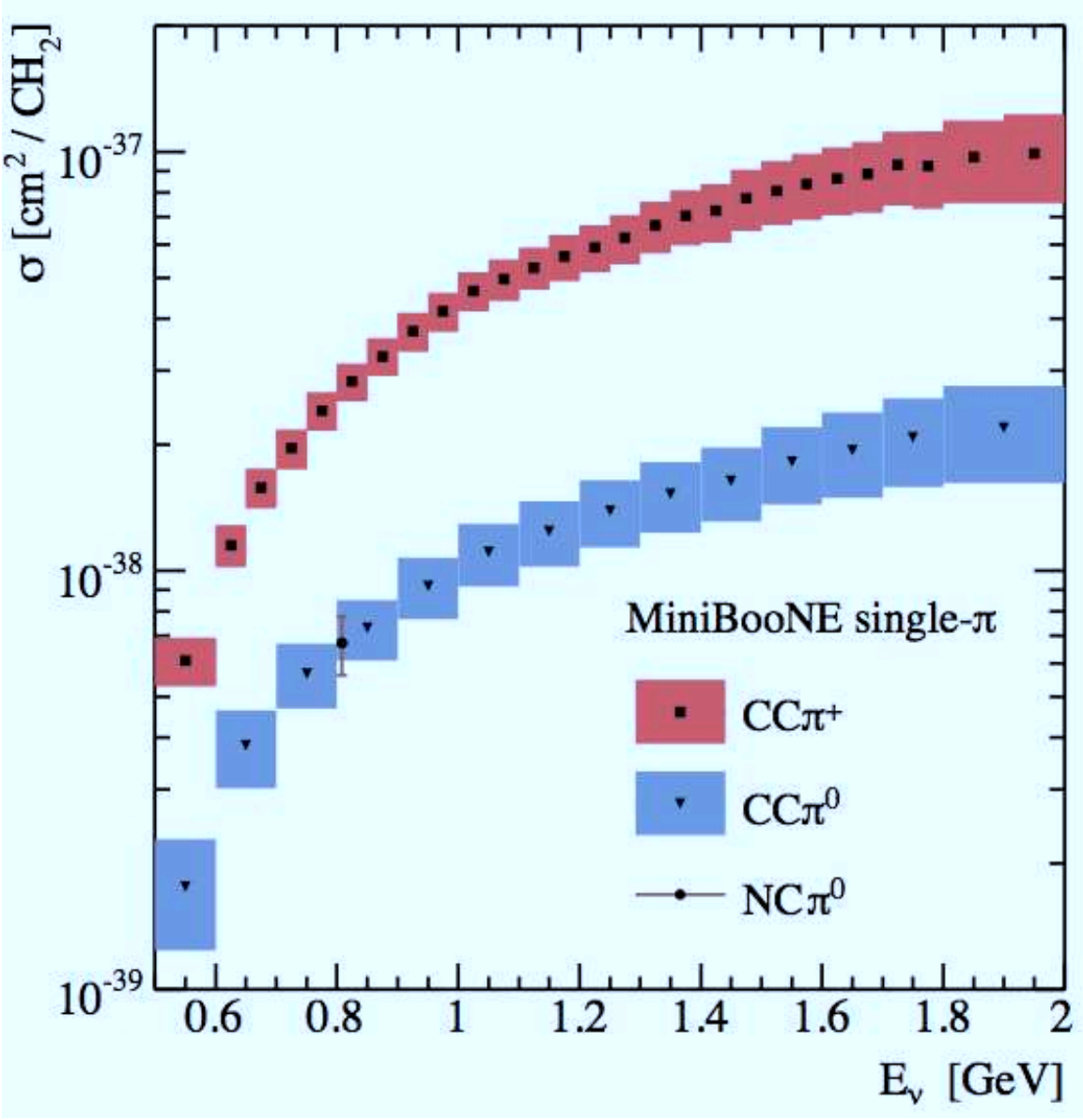

Figure 13: *The MiniBooNE single pion cross section measurements as a function of neutrino energy.*

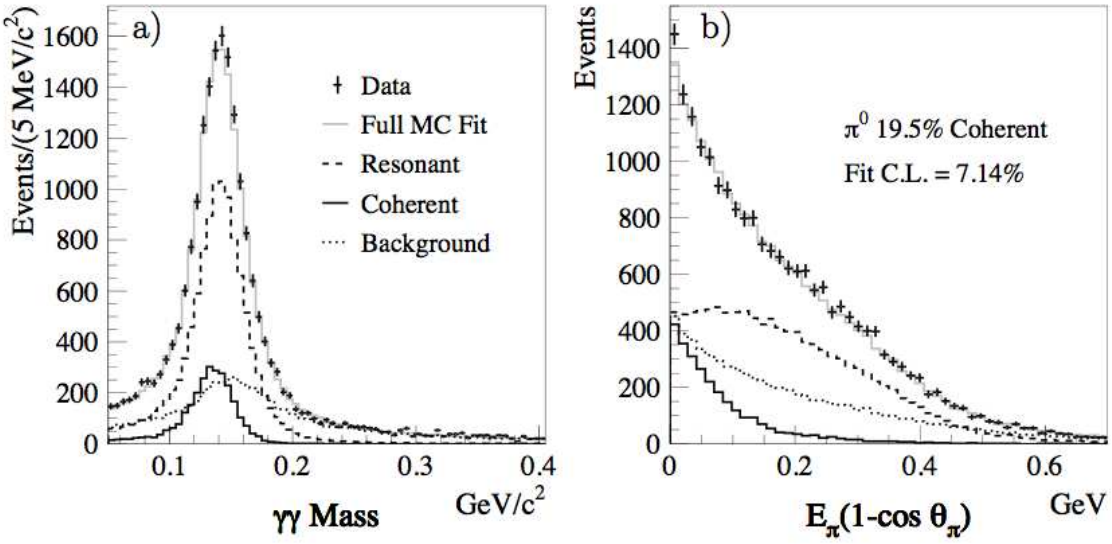

Figure 14: *The neutral-current π^0 $\gamma\gamma$ mass and $E_\pi(1-\cos\theta_\pi)$ distributions for data (points with error bars) compared to the MC simulation (histograms).*

3.3. Neutrino Oscillation Event Selection

MiniBooNE searches for $\nu_\mu \to \nu_e$ oscillations by measuring the rate of $\nu_e C \to e^- X$ CCQE events and testing whether the measured rate is consistent with the estimated background rate. To select candidate ν_e CCQE events, an initial selection is first applied: $>$ 200 tank hits, $<$ 6 veto hits, reconstructed time within the neutrino beam spill, reconstructed vertex radius $<$ 500 cm, and visible energy $E_{vis} > 140$ MeV. It is then required that the event vertex reconstructed assuming an outgoing electron and the track endpoint reconstructed assuming an outgoing muon occur at radii $<$ 500 cm and $<$ 488 cm, respectively, to ensure good event reconstruction and efficiency for possible muon decay electrons. Particle identification (PID) cuts are then applied to reject muon and π^0 events. Several improvements have been made to the neutrino oscillation data analysis since the initial data was published [22], including an improved background estimate, an additional fiducial volume cut that greatly reduces the background from events produced outside the tank (dirt events), and an increase in the data sample from 5.579×10^{20} POT to 6.462×10^{20} POT. A total of 89,200 neutrino events pass the initial selection, while 1069 events pass the complete event selection of the final analysis with $E_\nu^{QE} > 200$ MeV, where E_ν^{QE} is the

Table 1: *The expected number of events in the* $200 < E_\nu^{QE} < 300$ *MeV,* $300 < E_\nu^{QE} < 475$ *MeV, and* $475 < E_\nu^{QE} < 1250$ *MeV energy ranges from all of the significant backgrounds after the complete event selection of the final analysis. Also shown are the expected number of* ν_e *CCQE signal events for two-neutrino oscillations at the LSND best-fit solution.*

Process	$200-300$	$300-475$	$475-1250$
ν_μ CCQE	9.0	17.4	11.7
$\nu_\mu e \to \nu_\mu e$	6.1	4.3	6.4
NC π^0	103.5	77.8	71.2
NC $\Delta \to N\gamma$	19.5	47.5	19.4
Dirt Events	11.5	12.3	11.5
Other Events	18.4	7.3	16.8
ν_e from μ Decay	13.6	44.5	153.5
ν_e from K^+ Decay	3.6	13.8	81.9
ν_e from K_L^0 Decay	1.6	3.4	13.5
Total Background	186.8 ± 26.0	228.3 ± 24.5	385.9 ± 35.7
LSND Best-Fit Solution	7 ± 1	37 ± 4	135 ± 12

reconstructed neutrino energy.

3.4. Neutrino Oscillation Signal and Background Reactions

Table 1 shows the expected number of candidate ν_e CCQE background events with E_ν^{QE} between $200-300$ MeV, $300-475$ MeV, and $475-1250$ MeV after the complete event selection of the final analysis. The background estimate includes antineutrino events, representing $< 2\%$ of the total. The total expected backgrounds for the three energy regions are 186.8 ± 26.0 events, 228.3 ± 24.5 events, and 385.9 ± 35.7 events, respectively. For $\nu_\mu \to \nu_e$ oscillations at the best-fit LSND solution of $\Delta m^2 = 1.2$ eV^2 and $\sin^2 2\theta = 0.003$, the expected number of ν_e CCQE signal events for the three energy regions are 7 events, 37 events, and 135 events, respectively.

3.5. Neutrino Oscillation Results

Fig. 15 shows the reconstructed neutrino energy distribution for candidate ν_e data events (points with error bars) compared to the MC simulation (histogram) [22], while Fig. 2 shows the event excess as a function of reconstructed neutrino energy. Good agreement between the data and the MC simulation is obtained for $E_\nu^{QE} > 475$ MeV; however, an unexplained excess of electron-like events is observed for $E_\nu^{QE} < 475$ MeV. As shown in Fig. 2, the magnitude of the excess is very similar to what is expected from neutrino oscillations based on the LSND signal. Although the shape of the excess is not consistent with simple two-neutrino oscillations, more complicated oscillation models [5,6,33,7,34,35,36,37,38] or sterile neutrino decay [39] have shapes that may

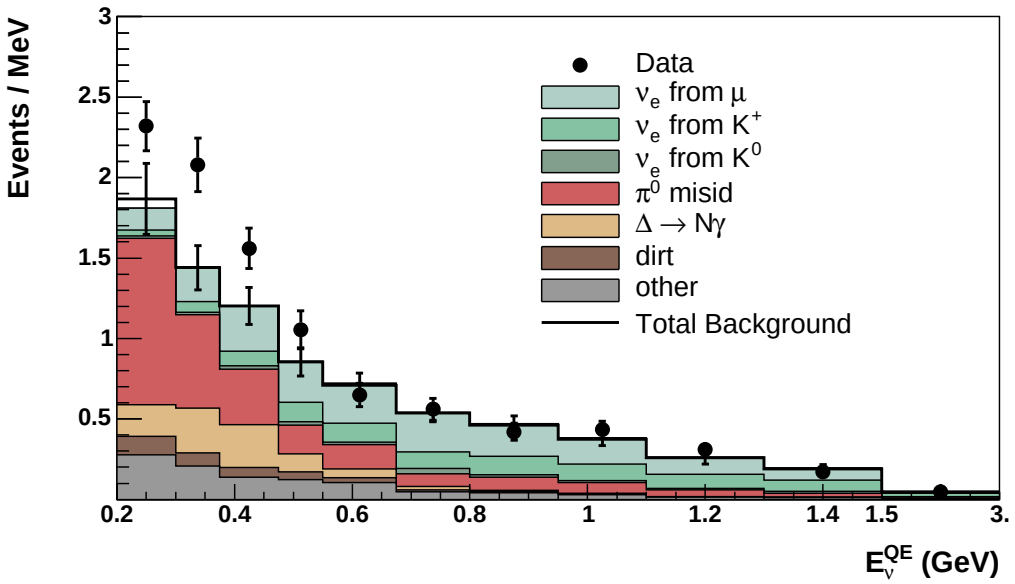

Figure 15: *The MiniBooNE reconstructed neutrino energy distribution for candidate ν_e data events (points with error bars) compared to the Monte Carlo simulation (histogram).*

be consistent with the LSND signal.

Table 2 shows the number of data, background, and excess events for different E_ν^{QE} ranges, together with the excess significance. For the final analysis, an excess of $128.8 \pm 20.4 \pm 38.3$ events is observed for $200 < E_\nu^{QE} < 475$ MeV. For the entire $200 < E_\nu^{QE} < 1250$ MeV energy region, the excess is $151.0 \pm 28.3 \pm 50.7$ events. As shown in Fig. 16, the event excess occurs for $E_{vis} < 400$ MeV, where E_{vis} is the visible energy.

Figs. 17 and 18 show the event excess as functions of Q^2 and $\cos(\theta)$ for events in the $300 < E_\nu^{QE} < 475$ MeV range, where Q^2 is determined from the energy and angle of the outgoing lepton and θ is the angle between the beam direction and the reconstructed event direction. Also shown in the figures are the expected shapes from $\nu_e C \rightarrow e^- X$ and $\bar{\nu}_e C \rightarrow e^+ X$ charged-current (CC) scattering and from the NC π^0 and $\Delta \rightarrow N\gamma$ reactions, which are representative of photon events produced by NC scattering. The NC scattering assumes the ν_μ energy spectrum, while the CC scattering assumes the transmutation of ν_μ into ν_e and $\bar{\nu}_e$, respectively. As shown in Table 3, the χ^2 values from comparisons of the event excess to the expected shapes are acceptable for all of the processes. However, any of the backgrounds in Table 3 would have to be increased by $> 5\sigma$ to explain the low-energy excess.

3.6. Antineutrino Oscillation Results

The same analysis that was used for the neutrino oscillation results is employed for the initial antineutrino oscillation results [2]. Fig. 19 shows the estimated neutrino fluxes for neutrino mode and antineutrino mode, respectively. The fluxes are fairly

Table 2: *The number of data, background, and excess events for different E_ν^{QE} ranges, together with the significance of the excesses in neutrino mode.*

Event Sample	Final Analysis
$200-300$ MeV	
Data	232
Background	$186.8 \pm 13.7 \pm 22.1$
Excess	$45.2 \pm 13.7 \pm 22.1$
Significance	1.7σ
$300-475$ MeV	
Data	312
Background	$228.3 \pm 15.1 \pm 19.3$
Excess	$83.7 \pm 15.1 \pm 19.3$
Significance	3.4σ
$200-475$ MeV	
Data	544
Background	$415.2 \pm 20.4 \pm 38.3$
Excess	$128.8 \pm 20.4 \pm 38.3$
Significance	3.0σ
$475-1250$ MeV	
Data	408
Background	$385.9 \pm 19.6 \pm 29.8$
Excess	$22.1 \pm 19.6 \pm 29.8$
Significance	0.6σ

Table 3: *The χ^2 values from comparisons of the neutrino event excess Q^2 and $\cos(\theta)$ distributions for $300 < E_\nu^{QE} < 475$ MeV to the expected shapes from various NC and CC reactions. Also shown is the factor increase necessary for the estimated background for each process to explain the low-energy excess and the corresponding number of sigma.*

Process	$\chi^2(cos\theta)$/9 DF	$\chi^2(Q^2)$/6 DF	Factor Increase
NC π^0	13.46	2.18	2.0 (6.8σ)
$\Delta \rightarrow N\gamma$	16.85	4.46	2.7 (18.4σ)
$\nu_e C \rightarrow e^- X$	14.58	8.72	2.4 (15.3σ)
$\bar{\nu}_e C \rightarrow e^+ X$	10.11	2.44	65.4 (41.0σ)

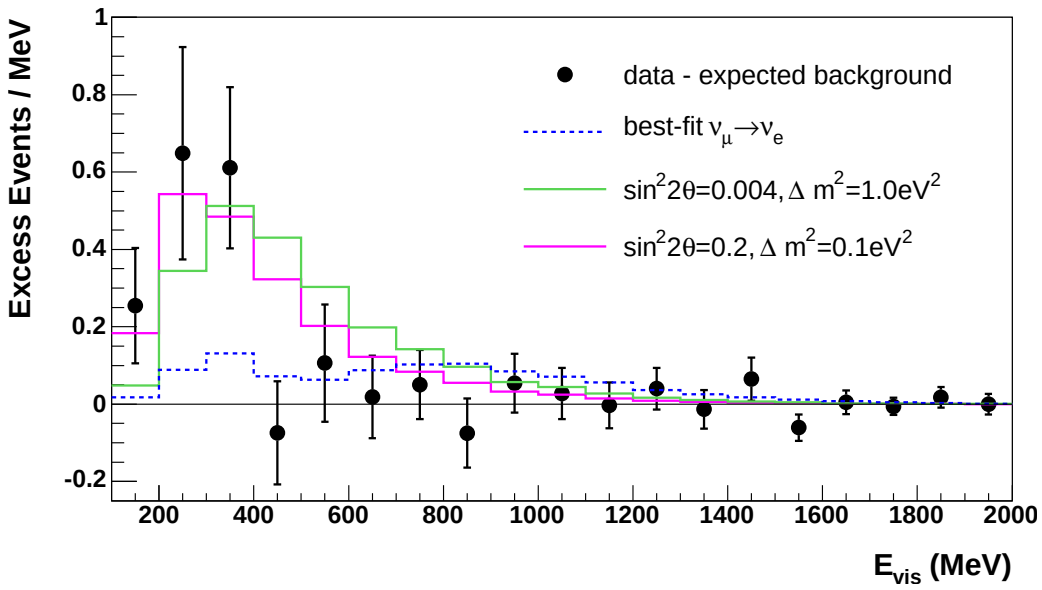

Figure 16: *The event neutrino excess as a function of E_{vis} for $E_\nu^{QE} > 200$ MeV. Also shown are the expectations from the best oscillation fit ($\sin^2 2\theta = 0.0017$, $\Delta m^2 = 3.14$ eV^2) and from neutrino oscillation parameters in the LSND allowed region. The error bars include both statistical and systematic errors.*

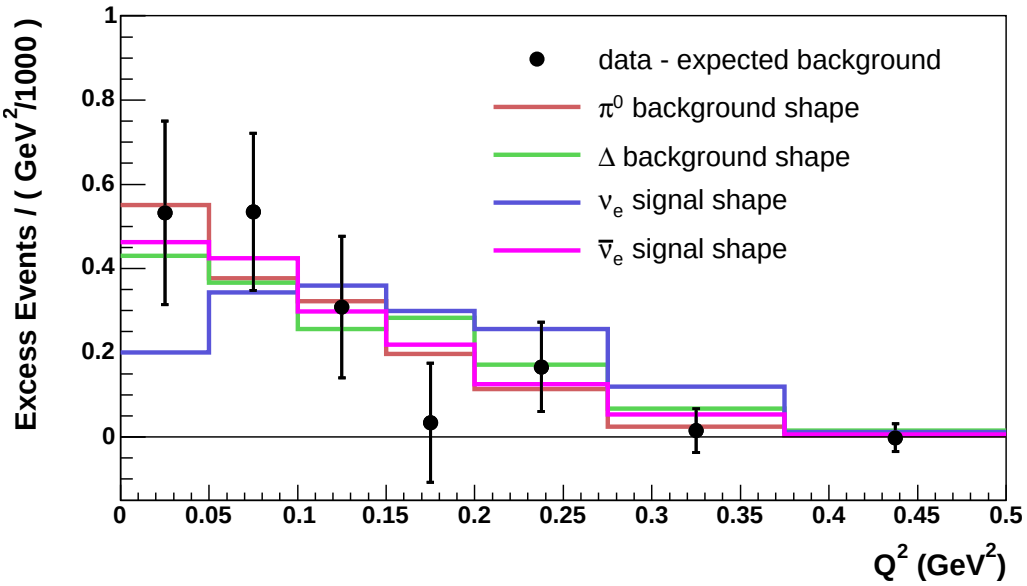

Figure 17: *The neutrino event excess as a function of Q^2 for $300 < E_\nu^{QE} < 475$ MeV.*

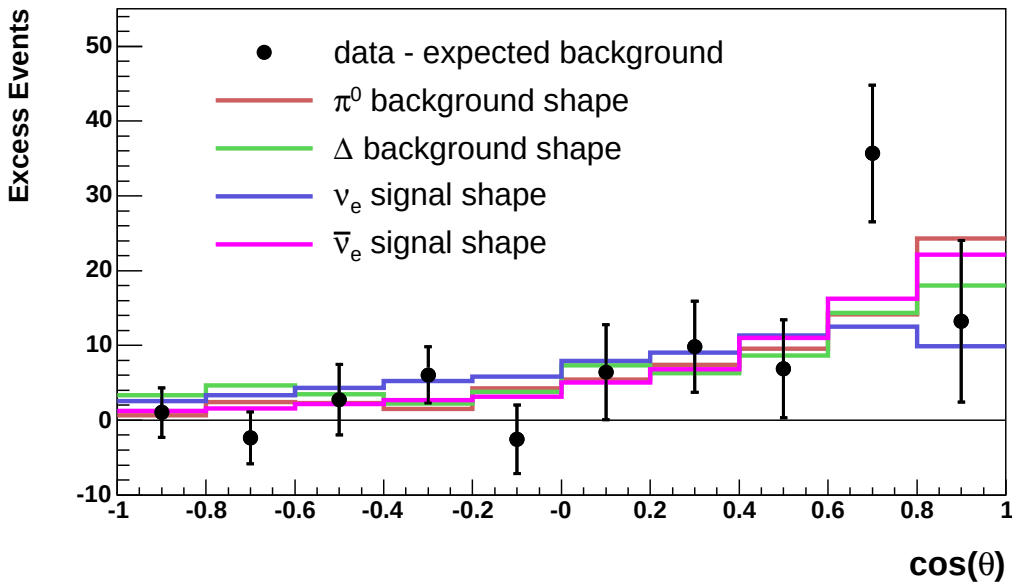

Figure 18: *The neutrino event excess as a function of* $\cos(\theta)$ *for* $300 < E_\nu^{QE} < 475$ *MeV.*

similar (the intrinsic electron-neutrino background is approximately 0.5% for both modes of running), although the wrong-sign contribution to the flux in antineutrino mode ($\sim 18\%$) is much larger than in neutrino mode ($\sim 6\%$). The average ν_e plus $\bar{\nu}_e$ energies are 0.96 GeV in neutrino mode and 0.77 GeV in antineutrino mode, while the average ν_μ plus $\bar{\nu}_\mu$ energies are 0.79 GeV in neutrino mode and 0.66 GeV in antineutrino mode. Also, as shown in Fig. 20, the estimated backgrounds in the two modes are very similar, especially at low energy.

At present, with 8.58E20 POT in antineutrino mode, MiniBooNE observes an event excess of ν_e and $\bar{\nu}_e$ candidates of $54.9 \pm 17.4 \pm 16.3$ events in the $200 < E_\nu < 1250$ MeV energy range, that is consistent with the antineutrino oscillations suggested by the LSND data [3]. Fig. 21 shows the energy distributions of the MiniBooNE $\bar{\nu}_e$ candidate events and the expected background, while Fig. 3 shows the excess of $\bar{\nu}_e$ candidate events in antineutrino mode. Figs. 4 and 5 show that the MiniBooNE oscillation allowed region and L/E distribution agree well with LSND.

4. BooNE

The BooNE experiment involves building a second detector at a cost of $\sim$ \$9M along the BNB at FNAL at a closer distance of $\sim$ 200 m. With two detectors, many of the systematic errors will cancel, as the neutrino flux varies as $1/r^2$ to good approximation, so that a ratio of events in the two detectors will provide a sensitive search for ν_e and $\bar{\nu}_e$ appearance and ν_μ and $\bar{\nu}_\mu$ disappearance. Furthermore, by comparing the rates for a NC reaction, either NC π^0 scattering or NC elastic scattering, a direct search for sterile neutrinos can be made. At a distance of 200

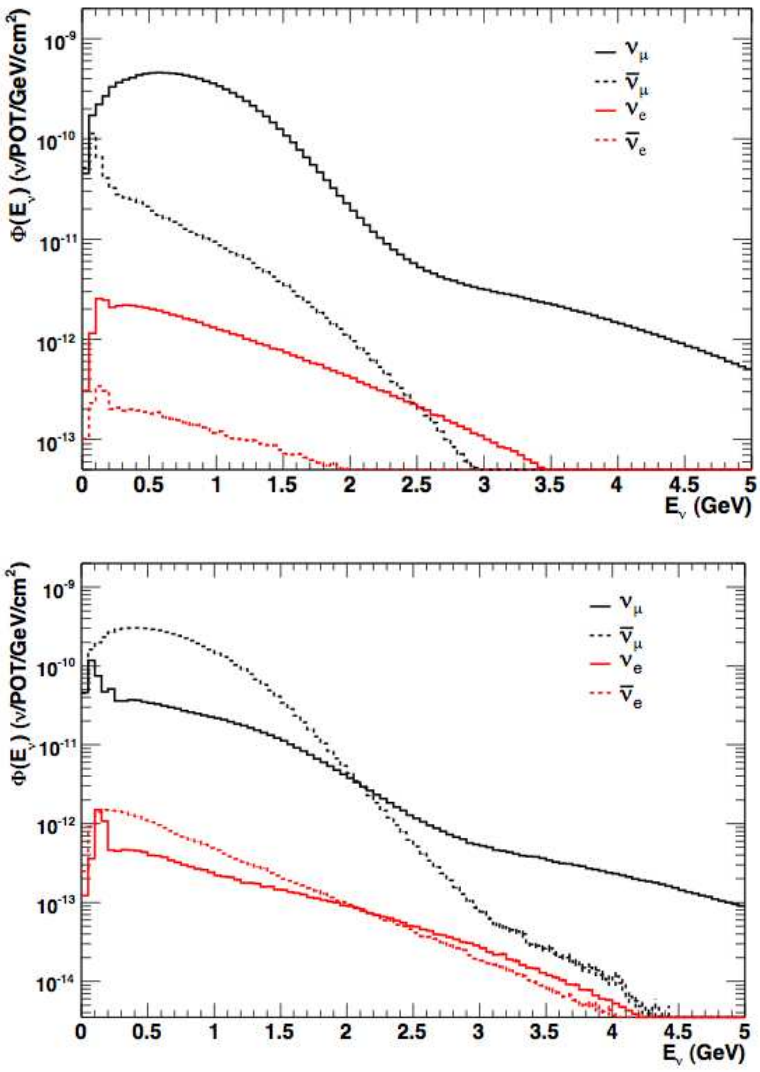

Figure 19: *The estimated neutrino fluxes for neutrino mode (top plot) and antineutrino mode (bottom plot).*

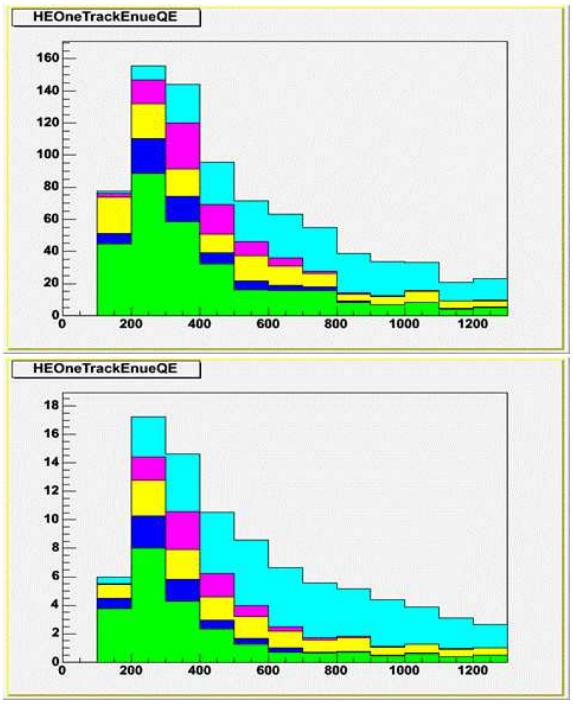

Figure 20: *The estimated backgrounds for the neutrino oscillation search in neutrino mode (top plot) and antineutrino mode (bottom plot). The π^0, $\Delta \rightarrow N\gamma$, intrinsic $\nu_e/\bar{\nu}_e$, external event, and other backgrounds correspond to the green, pink, light blue, blue, and yellow colors, respectively.*

m from the neutrino source, the event rate increases by a factor of $\sim$ 7 due to the dependence of the neutrino flux on distance. Therefore, after less than a year of running, the comparison of the event rates at the two locations will determine whether the excesses observed by MiniBooNE are due to neutrino oscillations. In addition, ν_μ and $\bar{\nu}_\mu$ disappearance will be searched for with high sensitivity in the $\Delta m^2 > 0.1$ eV^2 mass region. By comparing neutrino oscillations to antineutrino oscillations, BooNE will be able to search for CP violation in the lepton sector at short baseline ($\Delta m^2 > 0.1$ eV^2). For the sensitivities discussed below, it is assumed that the near detector will run for $\sim$ 1E20 POT in both neutrino mode and antineutrino mode.

4.1. Fluxes and Event Rates

This section gives a detailed comparison of the expected neutrino fluxes at the near (200 meter) and far (541 meters) positions. In the Booster neutrino beam (BNB), the primary beam is produced by the Fermilab 8 GeV rapid-cycling (15Hz) Booster accelerator, which produces 1.6 μs batches of protons with each batch containing approximately 4.5×10^{12} protons.

At that primary proton energy, there are only four significant species of neutrinos: ν_μ and $\bar{\nu}_\mu$ ($\sim$ 99.5%), and a small contamination ($\sim$ 0.5%) of ν_e and $\bar{\nu}_e$. There are two primary parent components to the fluxes: neutrinos from charged pion decays and

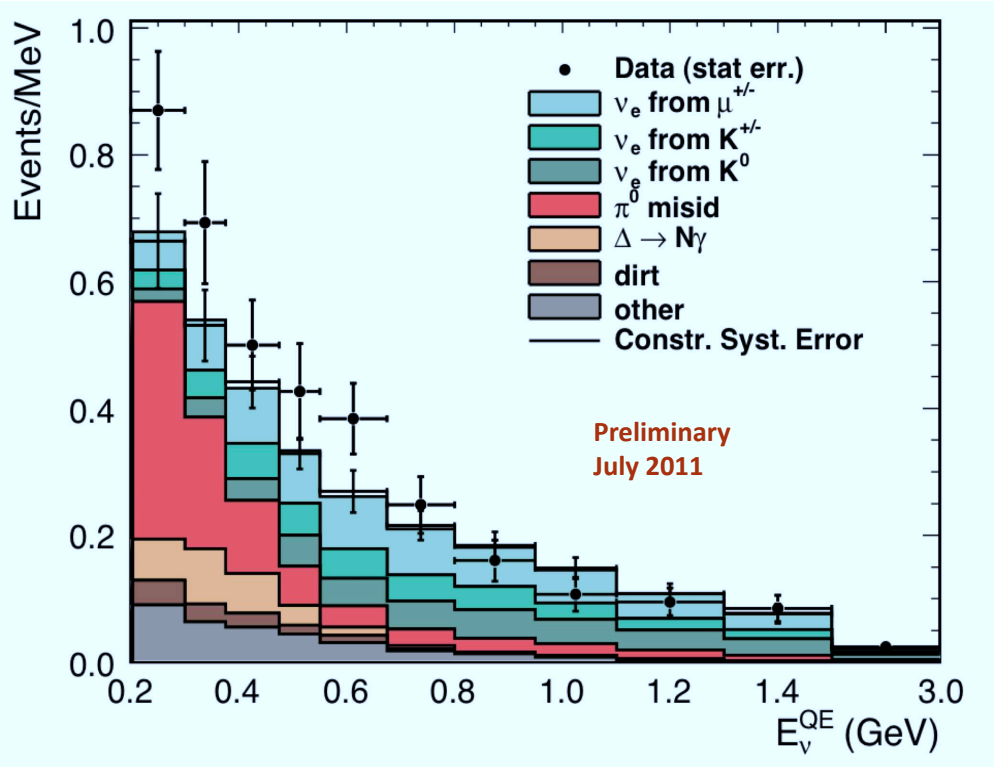

Figure 21: *The energy distributions of the MiniBooNE $\bar{\nu}_e$ candidate events and the expected background.*

neutrinos from kaon decays. The K^+ and K^0 component dominates the ν_μ spectrum above neutrino energies of 2.5 GeV, where a clear break is observed in the slope of the energy spectrum. The $\bar{\nu}_\mu$ spectra are mainly from charged pion decay, and the ν_e and $\bar{\nu}_e$ spectra are composed of two parts, muon decays and kaon decays.

The standard MiniBooNE Geant4 based beam simulation and decay program packages were used to generate fluxes[23]. Those packages include the transport of muon polarization (neglecting $g-2$ precession effects) and appropriate form factors in leptonic kaon decays. The primary production of pions by 8 GeV protons was measured by the HARP experiment[40] and is used as input in the simulation, while secondary interactions in the beamline are handled by standard Geant4 physics packages.

The fluxes shown here represent the spectrum of neutrinos that intersect a sphere of radius 610.6 cm, positioned at either the near or far location. The fluxes are "unoscillated" and therefore have only $\nu_\mu(\bar{\nu}_\mu)$and $\nu_e(\bar{\nu}_e)$ components. No matter effects in propagating the neutrinos to the detector are included, as they are expected to be small in the standard, 3-generation, active neutrino model (SνM).

Figs. 22, 23, 24, and 25 show the fluxes for the four neutrino species at the near and far locations, for both neutrino mode and antineutrino mode. Table 4 gives the same fluxes, integrated over neutrino energy, while Table 5 gives the average neutrino energy in each case. The neutrino fluxes are fairly constant over the detector area, even for the near locations.

In neutrino mode, the ν_μ flux near/far ratio is 7.5. Most of the near far ratios are between 7.0 and 8.0. Another characteristic of the near/far flux comparisions is that the average energy of the neutrinos in the near position is between 5 and 10 percent less than the corresponding average energy in the far position. This lower energy is expected since the near detector has a larger angular acceptance with respect to the neutrino target.

Fig. 26 shows the energy distribution for ν_μ CCQE events at the near (1.0×10^{20} POT) and far (6.462×10^{20} POT) locations for neutrino mode. The spectral differences are again due to the larger angular acceptance of the near detector. That larger decay angle translates to lower neutrino energies in the near detector, typically $\sim 10\%$ lower in the 200/541 meter comparison. This extrapolation is relatively straight forward as the angular divergence of the daughter neutrinos in the decays is much larger than the angular divergence of the decaying mesons themselves. For example, even at 3 GeV, daughter neutrinos from pion and kaon decays will have opening angles of $\sim$ 50 mrad and $\sim$ 150 mrad, respectively, while the allowed angular divergence of the beam tunnel is only $\sim$ 20 mrad.

Because of the nearly complete overlap in decay particle phase space that contributes to neutrinos in the near and far positions, we expect that uncertainties in the flux prediction will largely cancel when comparing the two event rates from the near and far positions. As systematic errors introduced by uncertainties in the detector efficiency and neutrino cross section will also largely cancel, the comparison of the two positions will allow a much-needed, accurate measurement of neutrino oscillation

effects in the Δm^2 range of 0.1-10 eV^2.

Table 4: *Integrated fluxes per POT for the various species of neutrinos at the near and far positions, for both neutrino mode and antineutrino mode.*

Fluxes $\nu/(cm^2\ POT)$

	ν mode		$\bar{\nu}$ mode	
ν species	Near	Far	Near	Far
ν_μ	7.49×10^{-8}	1.03×10^{-8}	8.12×10^{-9}	1.08×10^{-9}
$\bar{\nu}_\mu$	5.20×10^{-9}	6.52×10^{-10}	4.30×10^{-8}	5.77×10^{-9}
ν_e	4.50×10^{-10}	5.74×10^{-11}	9.5×10^{-11}	1.34×10^{-11}
$\bar{\nu}_e$	4.61×10^{-11}	6.00×10^{-12}	2.00×10^{-10}	2.53×10^{-11}

Table 5: *Average neutrino energies for the various species of neutrinos at the near and far positions, for both neutrino mode and antineutrino mode.*

Average ν energies (MeV)

	ν mode		$\bar{\nu}$ mode	
ν species	Near	Far	Near	Far
ν_μ	721	807	631	703
$\bar{\nu}_\mu$	412	461	593	649
ν_e	903	957	856	874
$\bar{\nu}_e$	917	971	677	716

4.2. Possible Scenarios for a Near Detector

The MiniBooNE detector has operated at a location of 541 meters from the Booster Neutrino Beam (BNB) target since September 1, 2002. The primary purpose of the experiment was to search for the transmutation, or oscillation, of muon neutrinos into electron neutrinos as they travel the $\sim$ 525 meters to the detector. The BNB was designed to produce a nearly pure beam of ν_μ, which provides an ideal setting to look for excess ν_e events. While the most sensitive neutrino oscillation experiments are two detector systems, which afford a comparison of similar detectors at two different distances, MiniBooNE was built as a single detector system in order to reduce costs. It was felt that the systematic error incurred by not building a second detector could be overcome by using internal measurements in the single detector. As ν_μ were not expected to oscillate significantly, it was planned to use their rate as a normalization for ν_e interactions, thus constraining backgrounds to ν_e events from oscillations.

The MiniBooNE proposal foresaw that a second detector at a different distance would be required to ascertain the nature of the signal, if a significant signal were observed in the single-detector setup. A second detector, located at a different distance

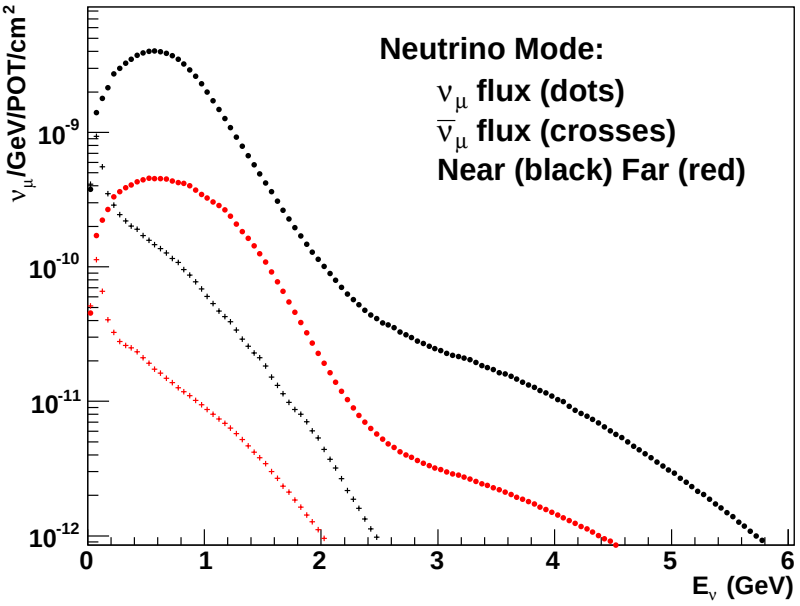

Figure 22: *The ν_μ and $\bar{\nu}_\mu$ fluxes at both the near and far locations in neutrino mode.*

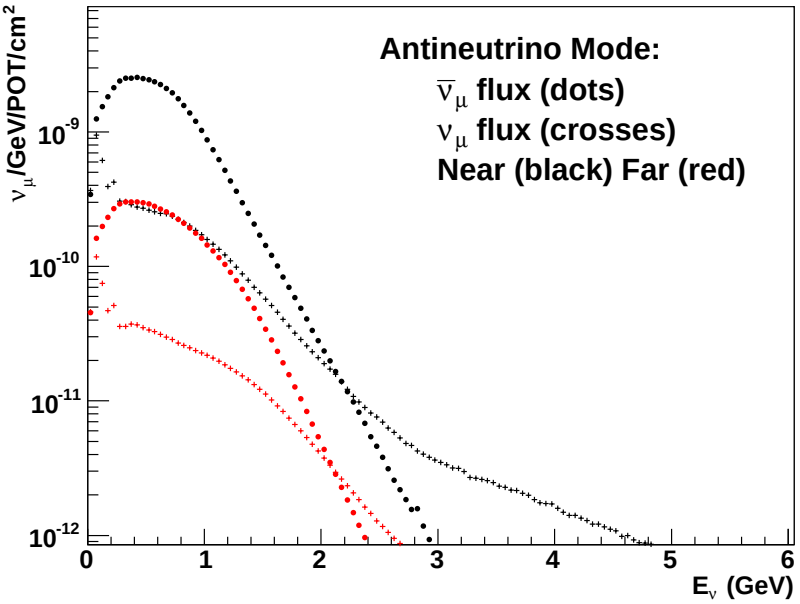

Figure 23: *The ν_μ and $\bar{\nu}_\mu$ fluxes at both the near and far locations in antineutrino mode.*

from the BNB target could potentially remove the large systematic errors that would complicate the interpretation of the MiniBooNE data.

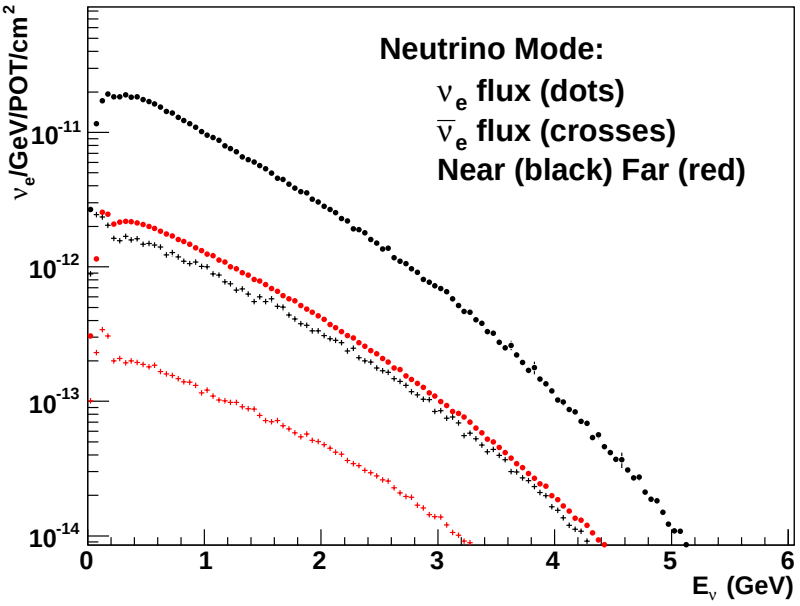

Figure 24: *The ν_e and $\bar{\nu}_e$ fluxes at both the near and far locations in neutrino mode.*

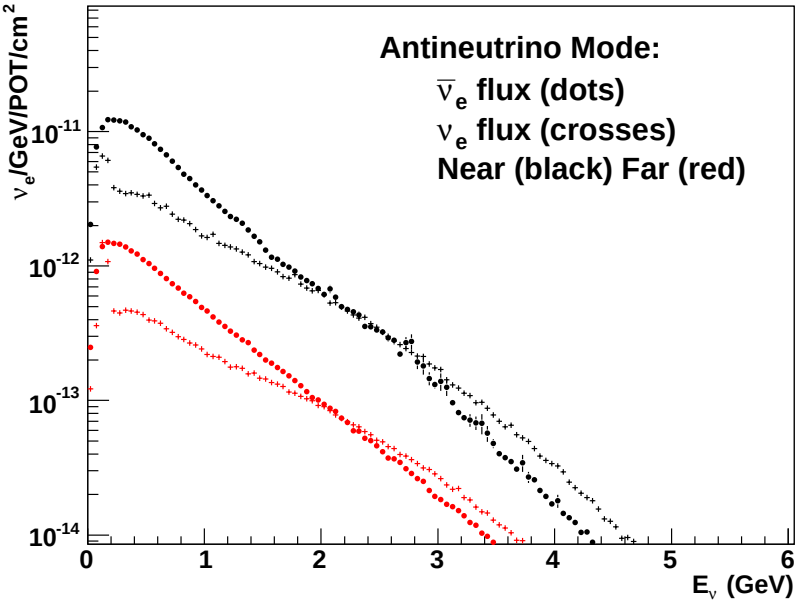

Figure 25: *The ν_e and $\bar{\nu}_e$ fluxes at both the near and far locations in antineutrino mode.*

There are a couple of possible routes to a more precise measurement which need to be considered: a new detector could be constructed at a near position; similarly,

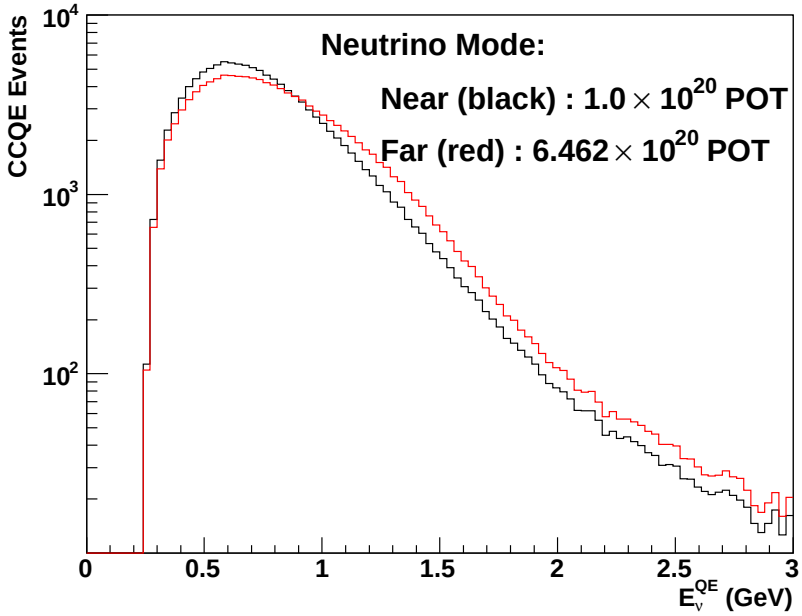

Figure 26: *The distribution of energies for reconstructed ν_μ CCQE events, at the near location with 1.0×10^{20} POT and at the far location with the current 6.462×10^{20} POT.*

a new detector could be constructed at a far position. Each of those possibilities has advantages and disadvantages.

4.2.1.

Near or Far?

The choice between constructing a near detector at ~ 200 meters and a far detector at ~ 1000 meters can be made based on expediency. For $\Delta m^2 < 2$ eV^2, a near detector will not see a large signal directly but can be used to accurately measure the expected backgrounds to any possible oscillation signal in the far detector. Those backgrounds, in both appearance and disappearance measurements, can be measured at $\sim$ 7-8 times the rate that the MiniBooNE detector accumulated data. Thus, a sample of neutrinos with statistics equivalent to MiniBooNE's existing data set of 6.462×10^{20} POT will only require $\sim$ 1.0×10^{20} POT and yield an $\sim 5\sigma$ result. An identical far detector, on the other hand, would also yield an $\sim 5\sigma$ result with $\sim$ 1.0×10^{20} POT, however the signal would only be $\sim$ 20 events on top of a background of $\sim$ 16 events. An unsatisfying, ambiguous result could occur with such low statistics.

4.2.2.

A New Detector

The location of the second detector at a near position $\sim$ 200 meters from the target is shown in Fig. 27. Choosing to construct an entirely new detector will allow for simultaneous operation of both the near and far detector and eliminate any fear, unfounded or not, that the neutrino beam has changed in character. The near BooNE detector will have the same dimensions as the MiniBooNE detector in order to reduce systematic uncertainties.

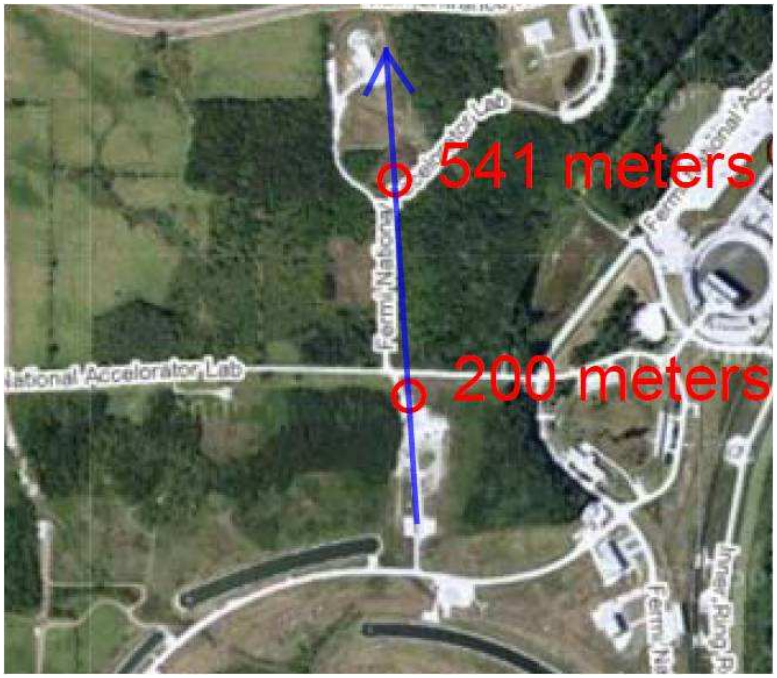

Figure 27: *An aerial view of Fermilab showing a possible location of a near detector at $\sim$ 200 meters. The blue arrow indicates the direction of the booster neutrino beam.*

4.3. Testing the Event Excesses

BooNE will be able to determine whether the event excesses are due to neutrino oscillations and will be able to test various hypotheses by comparing the excesses in neutrino and antineutrino modes. If the excesses are due to background, then the near detector will observe the same relative excess as the far detector. If the excesses are due to neutrino oscillations at low Δm^2, then no significant excesses will be observed in the near detector and the current low-energy neutrino excess in the far detector, assuming a 2.5% systematic error, will equal to $128.8 \pm 20.4 \pm 10.4$ events (5.6σ).

4.4. ν_e and $\bar{\nu}_e$ Appearance

The sensitivities for ν_e and $\bar{\nu}_e$ appearance were obtained by using the MiniBooNE

Monte Carlo simulation, assuming statistical errors with the expected MiniBooNE statistics (6.5E20 POT in neutrino mode and 1E21 POT in antineutrino mode) and a full error matrix with correlated and uncorrelated systematic errors. Also, we assume 2E20 POT in the near detector, equally divided between neutrino and antineutrino modes. Fig. 28 shows the estimated sensitivity for ν_e appearance for $E_\nu > 200$ MeV. Although simple two-neutrino oscillations have already been ruled out as an explanation of the LSND signal, it is interesting that the full LSND region is covered at the approximately 5σ level. Therefore, we would be able to determine whether or not the MiniBooNE low-energy excess is due to a more complicated oscillation mechanism at the ~ 1 eV^2 scale. Fig. 29 shows the estimated sensitivity for $\bar{\nu}_e$ appearance, where we assume that the error matrix is the same as for neutrinos. The sensitivity is worse than the ν_e appearance sensitivity due to the lower statistics and higher wrong-sign background in antineutrino mode; however, BooNE will still be able to cover the full LSND region at 90% CL and provide a direct test of LSND antineutrino oscillations.

4.5. ν_μ and $\bar{\nu}_\mu$ Disappearance

The sensitivities for ν_μ and $\bar{\nu}_\mu$ disappearance were obtained by using the MiniBooNE Monte Carlo simulation, assuming statistical errors with the expected MiniBooNE statistics (6.5E20 POT in neutrino mode and 1E21 POT in antineutrino mode) and a full error matrix with correlated and uncorrelated systematic errors. Also, we assume 2E20 POT in the near detector, equally divided between neutrino and antineutrino modes. Fig. 30 shows the estimated sensitivity for ν_μ disappearance for $E_\nu > 200$ MeV. A sensitivity of $\sim 3\%$ at 90% CL is obtained for $\Delta m^2 \sim 1$ eV^2. Figs. 31 shows the correponding limits for $\bar{\nu}_\mu$ disappearance, assuming no ν_μ disappearance and the same error matrix as for neutrinos. The $\bar{\nu}_\mu$ sensitivity is slightly worse than the ν_μ sensitivity due to the lower antineutrino statistics and the $\sim 1/3$ wrong-sign ν_μ component in antineutrino mode. A difference between ν_μ and $\bar{\nu}_\mu$ disappearance would be evidence for CPT violation or effective CPT violation.

4.6. Sterile Neutrino Search

If ν_μ or $\bar{\nu}_\mu$ disappearance is observed, then the NC π^0 and NC Elastic reactions can be used to determine whether the disappearance is due to oscillations into active or sterile neutrinos. Oscillations into sterile neutrinos will result in a suppression of events in the far detector, while oscillations into active neutrinos will result in no suppression. Due to the high statistics of the NC π^0 and NC Elastic event samples, the statistical error will be small compared to the systematic error. The sensitivity at 90% CL for oscillations into sterile neutrinos at $\Delta m^2 \sim 1$ eV^2 is estimated to be

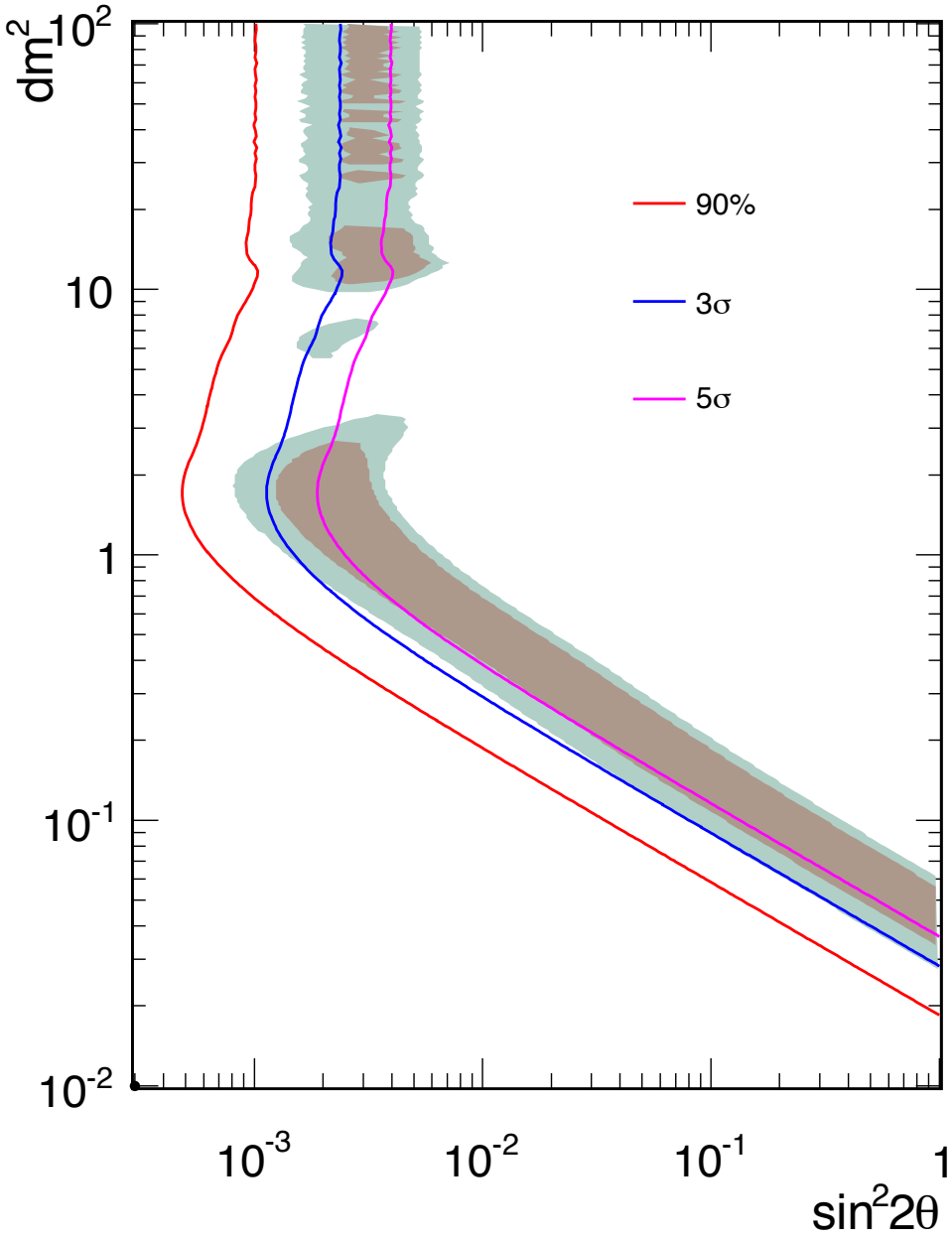

Figure 28: *The estimated BooNE sensitivity for ν_e appearance.*

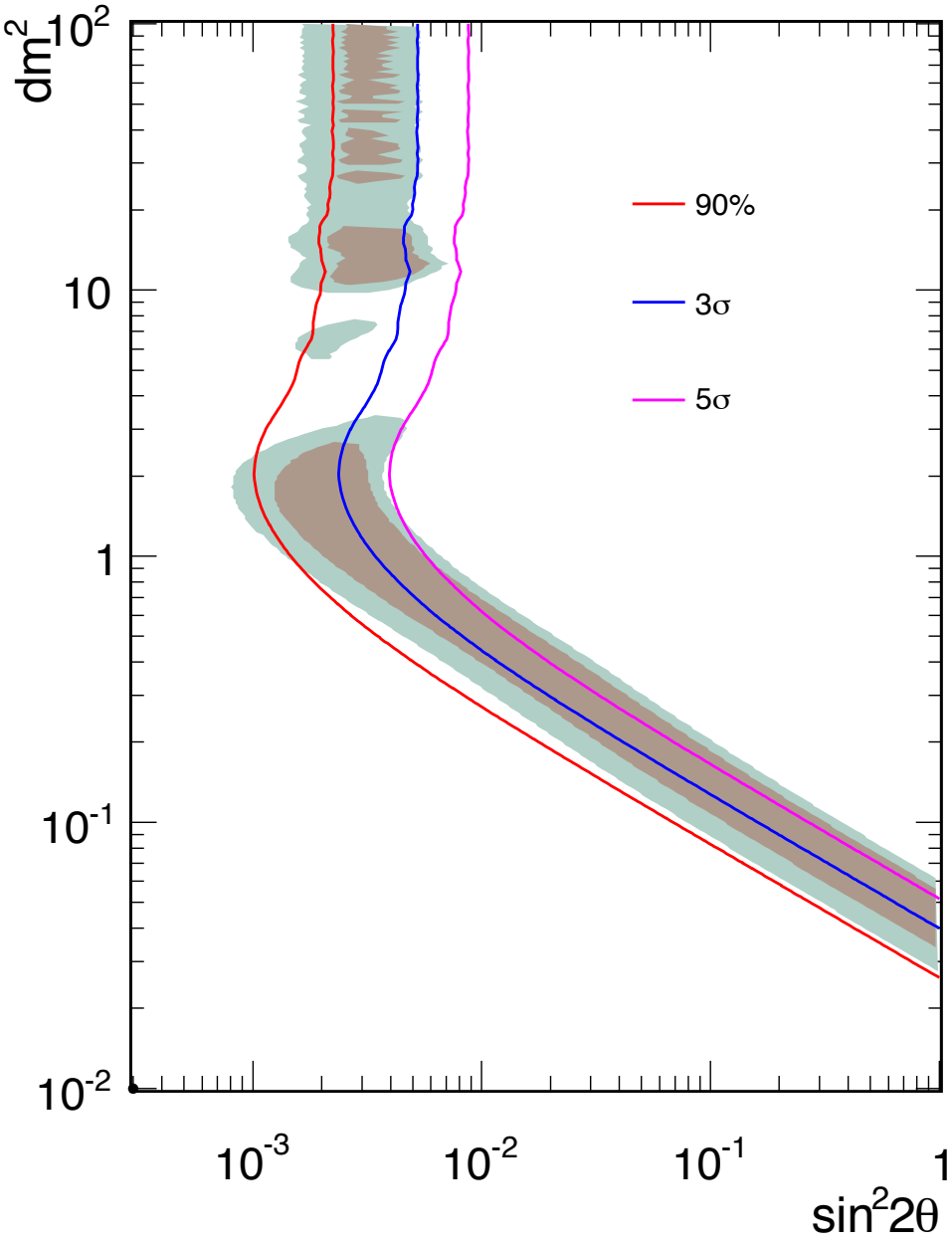

Figure 29: *The estimated BooNE sensitivity for $\bar{\nu}_e$ appearance.*

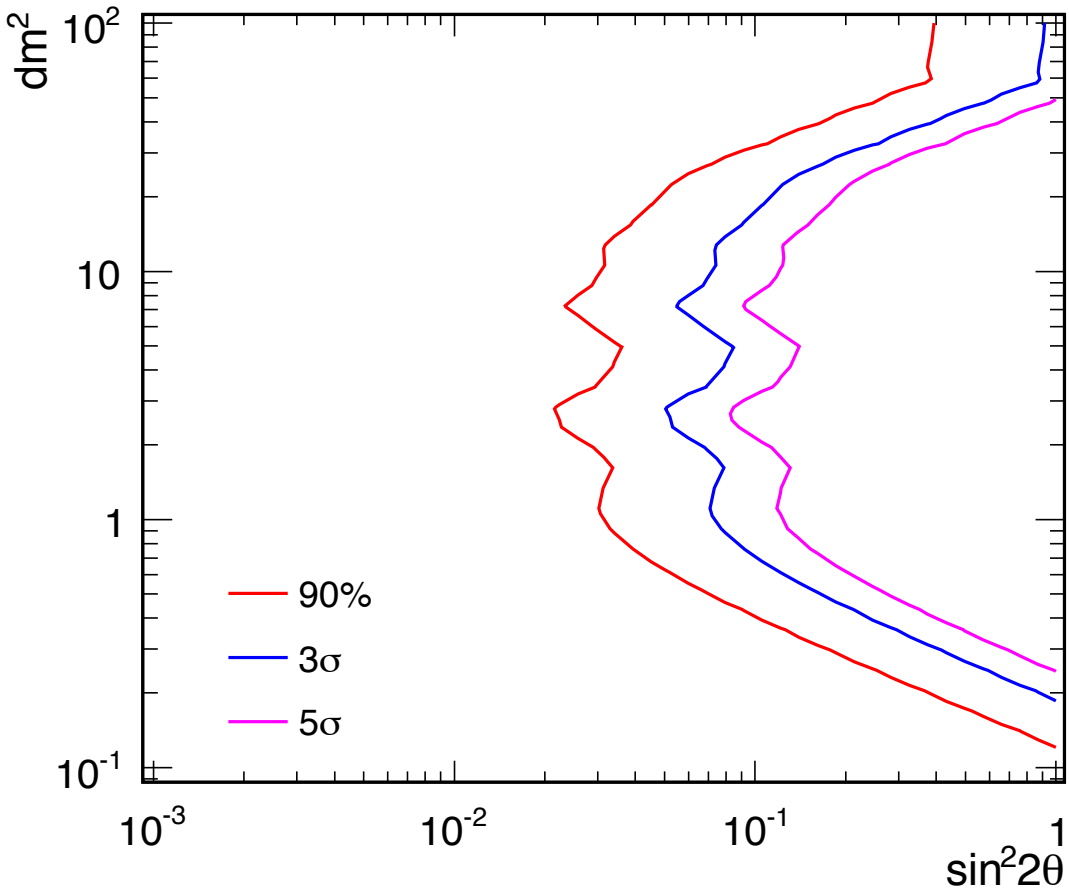

Figure 30: *The estimated BooNE sensitivity for ν_μ disappearance.*

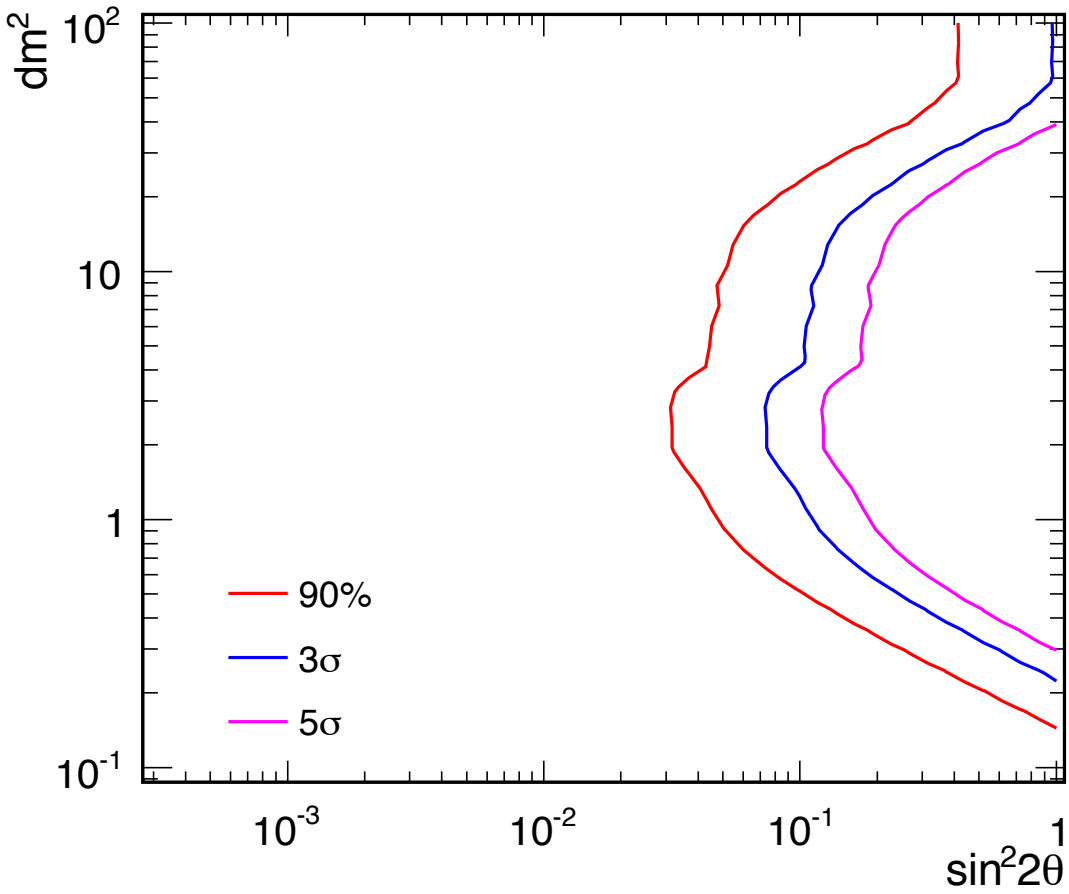

Figure 31: *The estimated BooNE sensitivity for $\bar{\nu}_\mu$ disappearance.*

Item	Cost ($K)
Tank	265.3
Support Structure	28.1
PMTs	2768.9
Preamps	30.6
Electronics	355.5
DAQ	67.2
Conventional Construction	4212.0
Plumbing	25.9
Oil	1283.6
Total	9037.2

Table 6: A breakdown of the cost estimate for constructing a second BooNE detector in a near location, including contingency and escalation.

$\sin^2 2\theta_{\mu\mu} \sim 3\%$ for neutrinos and $\sin^2 2\theta_{\mu\mu} \sim 5\%$ for antineutrinos.

4.7. Systematic Checks

With the high data rate available at the near position, a few month-long runs could aid in constraining the beam simulation and reduce systematic errors on the flux. This technique was employed successfully by the MINOS experiment to understand their neutrino flux. For example, data could be taken at serveral setting of the horn current and with the BNB 25m absorber in place.

5. Other Experiments

Another proposal that is capable of addressing these physics objectives at the ~ 1 eV^2 scale is a Letter of Intent to refurbish the CERN PS neutrino beam and build two liquid argon detectors [41]. However, the proposed BooNE experiment, with the existing BNB, should be able to obtain results prior to the CERN experiment.

6. Cost & Schedule Estimate

Table 6 shows a breakdown of the cost estimate for constructing a second BooNE detector in a near location. The estimate is based on the MiniBooNE as-built construction costs of $\sim$ \$6-7M. With contingency ($\sim 28\%$) and escalation (3% per year) the total estimated cost is \$9.0M, without project related labor. The total project cost with labor and project management will be $<$ \$20M. As much of the engineering was already done for the MiniBooNE experiment, the project could be streamlined and accomplished expeditiously. The BooNE construction is assumed to start in 2012 and last for 3 years. Table 7 shows a suggested schedule for the major milestones.

Milestone	Date
CD-0	3/26/12
CD-1	7/17/12
CD-2	9/26/12
CD-3 Construction Start	5/24/13
Tank Complete	8/1/13
Conventional Construction Complete	12/3/13
Electronics Complete	10/19/13
DAQ Start	5/24/13
PMTs Installed	4/24/14
CD-4	5/26/14

Table 7: A suggested schedule for the major milestones.

7. References

1) A. A. Aguilar-Arevalo *et al.* , Phys. Rev. Lett. **102**, 101802 (2009).
2) A. Aguilar-Arevalo *et al.*, Phys. Rev. Lett. 105, 181801 (2010).
3) C. Athanassopoulos *et al.*, Phys. Rev. Lett. 75, 2650 (1995); 77, 3082 (1996); 81, 1774 (1998); A. Aguilar *et al.*, Phys. Rev. D 64, 112007 (2001).
4) G. Mention *et al.*, Phys. Rev. D 83, 073006 (2011).
5) G. Karagiorgi *et al.*, Phys. Rev. D 80, 073001 (2009).
6) Joachim Kopp, Michele Maltoni, and Thomas Schwetz, Phys. Rev. Lett. 107, 091801 (2011).
7) Carlo Giunti and Marco Laveder, [arXiv:1107.1452]; Phys. Rev. D 83 053006 (2011); Phys. Rev. D 82 093916 (2010); Phys. Rev. D 82 113009 (2010).
8) B. T. Cleveland *et al.*, Astrophys. J. 496, 505 (1998).
9) J. N. Abdurashitov *et al.*, Phys. Rev. C 60, 055801 (1999).
10) W. Hampel *et al.*, Phys. Lett. B 447, 127 (1999).
11) S. Fukuda *et al.*, Phys. Lett. B 539, 179 (2002).
12) Q. R. Ahmad *et al.*, Phys. Rev. Lett. 87, 071301 (2001); Q. R. Ahmad *et al.*, Phys. Rev. Lett. 89, 011301 (2002); S. N. Ahmed *et al.*, Phys. Rev. Lett. 92, 181301 (2004).
13) K. Eguchi *et al.*, Phys. Rev. Lett. 90, 021802 (2003); T. Araki *et al.*, Phys. Rev. Lett. 94, 081801 (2005).
14) K. S. Hirata *et al.*, Phys. Lett. B 280, 146 (1992); Y. Fukuda *et al.*, Phys. Lett. B 335, 237 (1994).
15) Y. Fukuda *et al.*, Phys. Rev. Lett. 81, 1562 (1998).
16) W. W. M. Allison *et al.*, Phys. Lett. B 449, 137 (1999).
17) M. Ambrosio *et al.*, Phys. Lett. B 517, 59 (2001).
18) M. H. Ahn *et al.*, Phys. Rev. Lett. 90, 041801 (2003).
19) D. G. Michael *et al.*, Phys. Rev. Lett. 97, 191801 (2006); P. Adamson *et al.*, Phys. Rev. Lett. 101, 131802 (2008). P. Adamson *et al.*, Phys. Rev. Lett. 106, 181801 (2011).
20) T. Katori, A. Kostelecky and R. Tayloe, Phys. Rev. D 74, 105009 (2006).
21) Jorge S. Diaz and Alan Kostelecky, [arXiv:1108.1799].
22) A. Aguilar-Arevalo *et al.*, Phys. Rev. Lett. 98, 231801 (2007); A. Aguilar-Arevalo *et al.*, Phys. Rev. Lett. 102, 101802 (2009).

23) A. Aguilar-Arevalo *et al.*, Phys. Rev. D **79**, 072002 (2009).
24) A. Aguilar-Arevalo *et al.*, Nucl. Instr. Meth. **A599**, 28 (2009).
25) A. Aguilar-Arevalo *et al.*, Phys. Rev. D **81**, 092005 (2010).
26) J. Carlson *et al.*, Phys. Rev. C **65**, 024002 (2002).
27) M. Martini *et al.*, Phys. Rev. C **80**, 065001 (2009).
28) J. Nieves, I. Ruiz Simo, and M. J. Vicente Vacas, [arXiv:1106.5374].
29) A. Aguilar-Arevalo *et al.*, Phys. Rev. D **82**, 092005 (2010).
30) A. Aguilar-Arevalo *et al.*, Phys. Rev. D **83**, 052007 (2011).
31) A. Aguilar-Arevalo *et al.*, Phys. Rev. D **83**, 052009 (2011).
32) A. Aguilar-Arevalo *et al.*, Phys. Lett. 664B, 41 (2008); Phys. Rev. D **81**, 013005 (2010).
33) Michele Maltoni and Thomas Schwetz, Phys. Rev. D 76, 093005 (2007); [arXiv:0705.0197].
34) Heinrich Paes, Sandip Pakvasa, Thomas J. Weiler, Phys. Rev. D 72, 095017 (2005); [arXiv:hep-ph/0504096].
35) T. Goldman, G. J. Stephenson Jr., and B. H. J. McKellar, Phys. Rev. D 75, 091301 (2007).
36) Ann E. Nelson and Jonathan Walsh, [arXiv:0711.1363].
37) Sebastian Hollenberg and Heinrich Paes, [arXiv:0904.2167].
38) Evgeny Akhmedov and Thomas Schwetz, JHEP 1010, 115 (2010).
39) S. N. Gninenko, Phys. Rev. D 83, 093010 (2011); [arXiv:1107.0279].
40) M. G. Catanesi *et al.*, Eur. Phys. J. C **52**, 29 (2007) [arXiv:hep-ex/0702024].
41) B. Baibussinov *et al.*, [arXiv:0909.0355].